C^1 Natural Neighbor Interpolant for Partial Differential Equations

N. Sukumar and B. Moran
Department of Civil Engineering
Northwestern University
Evanston, Illinois 60201

Natural neighbor coordinates [20] are optimum weighted-average measures for an irregular arrangement of nodes in $\mathbb{R}^n$. [26] used the notion of Bézier simplices in natural neighbor coordinates $\mathbf{\Phi}$ to propose a C^1 interpolant. The C^1 interpolant has quadratic precision in $\Omega \subset \mathbb{R}^2$, and reduces to a cubic polynomial between adjacent nodes on the boundary $\partial\Omega$. We present the C^1 formulation and propose a computational methodology for its numerical implementation (Natural Element Method) for the solution of partial differential equations (PDEs). The approach involves the transformation of the original Bernstein basis functions $B_{\mathbf{i}}^3(\Phi)$ to new shape functions $\Psi(\Phi)$, such that the shape functions $\psi_{3I-2}(\Phi), \psi_{3I-1}(\Phi)$, and $\psi_{3I}(\Phi)$ for node I are directly associated with the three nodal degrees of freedom w_I, θ_{I_x}, and θ_{I_y}, respectively. The C^1 shape functions interpolate to nodal function and nodal gradient values, which renders the interpolant amenable to application in a Galerkin scheme for the solution of fourth-order elliptic PDEs. Results for the biharmonic equation with Dirichlet boundary conditions are presented. The generalized eigenproblem is studied to establish the ellipticity of the discrete biharmonic operator, and consequently the stability of the numerical method. © 1999 John Wiley & Sons, Inc. Numer Methods Partial Differential Eq 15: 417–447, 1999

Keywords: C^1 interpolant; Bernstein–Bézier polynomials; natural neighbor coordinates; natural element method; biharmonic equation; plate bending

I. INTRODUCTION

The ability to develop C^1 interpolants over an arbitrary bounded domain Ω is a much researched and far from trivial task. The higher-order smoothness or continuity requirement of interpolants is of interest, because such classes of trial functions are necessary in a Galerkin formulation for the solution of higher-order elliptic partial differential equations (PDEs)—C^1 trial functions for the biharmonic (fourth-order) equation, with Kirchhoff plate bending in elasticity being a notable application and a case in point. In a general framework, C^1 continuity on the primary variable is required, when the balance laws of a continuum can be cast in variational form and second-order derivatives of the primary variable appear in the variational statement. For example, in the

CCC 0749-159X/99/040417-31

problem of nucleation of a solid–solid phase transformation based on an energy functional that is dependent on the strain and strain gradients, the Galerkin implementation requires C^1-continuous trial functions [1].

In the realm of finite elements, one of the first C^1 interpolants developed was the Clough–Tocher finite element [2, 3] and in subsequent years many of its variants have emerged [4, 5]. Some of the other early developments in conforming triangular finite elements are due to de Veubeke [6], Irons [7], Bell [8], and Powell and Sabin [9]. The construction of finite elements with C^1-continuity is, in general, unwieldy with significant complexity arising in the construction of the interpolant; moreover, the need to include first-order and second-order derivatives as additional nodal degrees of freedom tends to adversely affect the numerical solution. A general overview of the finite element interpolation problem for minimally C^1-continuous polynomial interpolants is presented by Peano [10]. Local C^k ($k > 0$) interpolants on a regular grid are readily constructed using splines. Lai and Wenston [11] use continuously differentiable C^1 cubic splines for the solution of elliptic partial differential equations. For irregularly spaced data, an attractive choice for constructing C^k functions is to use C^k weight functions that have compact support; for example, Shepard's interpolant [12], compactly supported radial basis functions [13], or moving least squares (MLS) approximants [14]. These approaches lend themselves readily to curve and surface data fitting. Wendland [15] proposes a Galerkin method using radial basis functions, and Fasshauer [16] presents a review of meshless radial basis functions for the numerical solution of PDEs. In the application of MLS approximants to PDEs, certain issues do pose problems; for example, the noninterpolating property of MLS approximants leads to complications in the imposition of Dirichlet boundary conditions in a Galerkin scheme for the biharmonic equation [17, 18]. Moreover, the numerical solution is sensitive to both the weight function and its radius of support. A partial resolution to the above shortcomings is met by using smooth interpolating trial functions, as evidenced by the work of Donning [19] in which cardinal splines are used in a displacement-based Galerkin scheme to solve shear-deformable thick as well as thin beam and plate problems using Mindlin–Reissner theory.

A relatively new result in interpolation theory [20] has recently led to the development of a novel approach for the representation of multivariate data and to the solution of partial differential equations of physics using a meshless method [21, 22]. This method, termed the Natural Element Method (NEM), shows significant promise for problems in solid mechanics [23]. In the natural element method, the trial and test functions are constructed using natural neighbor interpolants [20]. These interpolants are local in character, and are based on the Voronoi tessellation [24] of the set of nodes. As opposed to finite elements, there is no notion of element connectivity in the construction of the NEM interpolant, and, in this context, the numerical implementation is viewed as a meshless or meshfree method [25].

In this article, we present the computational implementation of a natural neighbor-based C^1 interpolant for the solution of PDEs. Farin [26] constructed a C^1 interpolant by embedding Sibson's natural neighbor coordinates in the Bernstein–Bézier surface representation of a cubic simplex. The C^1 NEM interpolant that we propose is based on a transformation of Farin's interpolant, and, as a result, interpolation to nodal function and nodal gradient values is realized. This renders the C^1 NEM interpolant amenable to use in a Galerkin scheme for the solution of fourth-order elliptic PDEs.

The outline of this article is as follows. In Section II, a concise description of Sibson's natural neighbor interpolant is presented. In Section III, we first outline Farin's natural neighbor-based C^1 interpolant; then, we present the methodology used to derive the C^1 NEM shape functions that are used in this article. The construction, properties, and numerical computations of the C^1 NEM shape functions are discussed in Section IV. In Section V, the governing equations for the

biharmonic equation together with the Galerkin formulation for NEM are described. In Section VI, two applications of NEM for the biharmonic equation with Dirichlet boundary conditions are presented. Finally, in Section VII, some concluding remarks are mentioned.

II. NATURAL NEIGHBOR INTERPOLATION

In this section, we briefly touch upon the foundations of Sibson's natural neighbor coordinates (shape functions), which are used in the natural element method. For a more in-depth discussion on the Sibson interpolant and its application to second-order partial differential equations in mechanics, the interested reader can refer to Braun and Sambridge [22] and Sukumar et al. [23], and the references therein.

Consider a set of distinct nodes $N = \{n_1, n_2, \ldots, n_M\}$ in $\mathbb{R}^2$. The Voronoi diagram with its dual Delaunay triangulation is one of the most fundamental and useful geometric constructs that defines an irregular set of points (nodes). Natural neighbor coordinates, which were introduced by Sibson [20], are constructed on the basis of the underlying Voronoi tessellation for the nodal set N. The Voronoi diagram (or 1*st*-order Voronoi diagram) of the set N is a subdivision of the plane into regions T_I (Voronoi polygons) given by

$$T_I = \{\mathbf{x} \in \mathbb{R}^2 \colon d(\mathbf{x}, \mathbf{x}_I) < d(\mathbf{x}, \mathbf{x}_J) \quad \forall\, J \neq I\}, \tag{2.1}$$

where $d(\mathbf{x}_I, \mathbf{x}_J)$, the Euclidean metric, is the distance between $\mathbf{x}_I$ and $\mathbf{x}_J$.

The Voronoi diagram for a set of seven nodes is shown in Fig. 1(a). In Fig. 1(b), a point $\mathbf{x}$ is introduced into the Voronoi diagram of the set N. If $\mathbf{x}$ is tessellated along with the nodal set N, then, in the newly constructed triangulation based on N and $\mathbf{x}$, the natural neighbors of $\mathbf{x}$ are those nodes that are connected by a Delaunay edge to $\mathbf{x}$. The natural neighbor coordinates (shape functions) of $\mathbf{x}$ with respect to a natural neighbor I are defined as the ratio of the area of overlap of their Voronoi cells to the total area of the Voronoi cell of $\mathbf{x}$:

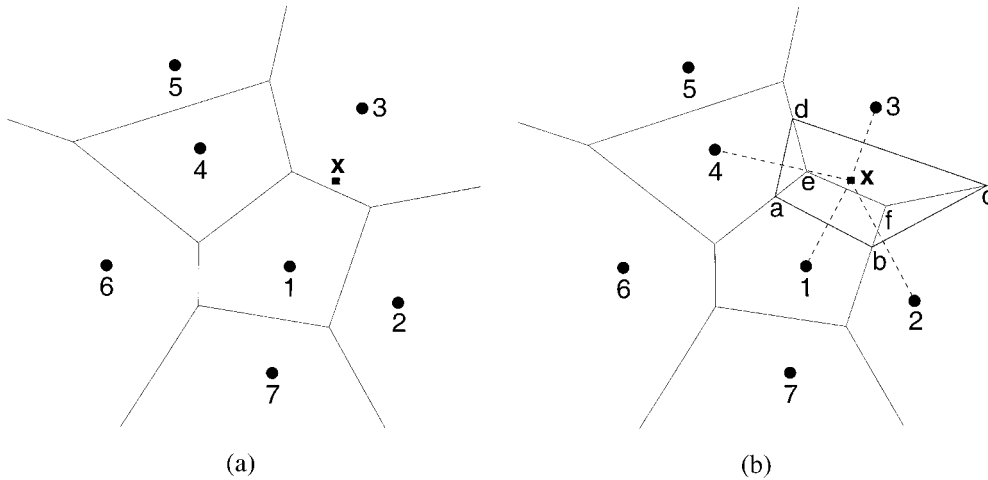$$\phi_I(\mathbf{x}) = \frac{A_I(\mathbf{x})}{A(\mathbf{x})}, \tag{2.2a}$$

FIG. 1. Construction of natural neighbor coordinates. (a) original Voronoi diagram and $\mathbf{x}$, and (b) 1*st*-order and 2*nd*-order Voronoi cells about $\mathbf{x}$.

$$A(\mathbf{x}) = \sum_{J=1}^{n} A_J(\mathbf{x}), \tag{2.2b}$$

where I ranges from 1–n in Eq. (2.2a). If the point $\mathbf{x}$ approaches a node $(\mathbf{x} \to \mathbf{x}_I)$, $\phi_I(\mathbf{x}) = 1$, and all other shape functions are zero. By this fact, and by construction, the properties of positivity, interpolation, and partition of unity directly follow:

$$0 \leq \phi_I(\mathbf{x}) \leq 1, \quad \phi_I(\mathbf{x}_J) = \delta_{IJ}, \quad \sum_{I=1}^{n} \phi_I(\mathbf{x}) = 1 \ \text{ in } \Omega. \tag{2.3}$$

In addition to the above, natural neighbor shape functions satisfy the local coordinate property [20], namely

$$\mathbf{x} = \sum_{I=1}^{n} \phi_I(\mathbf{x})\mathbf{x}_I, \tag{2.4}$$

which indicates that the shape functions can exactly reproduce the geometrical coordinates. The above equation in conjunction with the partition of unity property in Eq. (2.3) imply that linear completeness is satisfied by the $C^0(\Omega)$ natural neighbor interpolant.

On using Eq. (2.2a), we can write the first- and second-order derivatives of natural neighbor shape functions as

$$\phi_{I,\alpha}(\mathbf{x}) = \frac{A_{I,\alpha}(\mathbf{x}) - \phi_I(\mathbf{x})A_{,\alpha}(\mathbf{x})}{A(\mathbf{x})}, \tag{2.5a}$$

$$\phi_{I,\alpha\beta}(\mathbf{x}) = \frac{A_{I,\alpha\beta}(\mathbf{x}) - \phi_I(\mathbf{x})A_{,\alpha\beta}(\mathbf{x}) - \phi_{I,\beta}(\mathbf{x})A_{,\alpha}(\mathbf{x}) - \phi_{I,\alpha}(\mathbf{x})A_{,\beta}(\mathbf{x})}{A(\mathbf{x})}, \tag{2.5b}$$

where Greek indices α and β are used to denote derivatives along coordinate directions x and y. The geometric algorithm proposed by Watson [27] is used to compute the natural neighbor shape functions and its derivatives.

III. C^1 NATURAL NEIGHBOR INTERPOLANT

Farin [26] has proposed a C^1 interpolant based on Sibson's original C^0 natural neighbor interpolant. By embedding Sibson's coordinate in the Bernstein–Bézier representation of a cubic simplex, a C^1 interpolant is realized. Bernstein–Bézier patches and related concepts are widely used in the area of surface approximation and in the field of computer-aided geometric design [28]. A review article on triangular Bernstein–Bézier surfaces can be found in Farin [29], and a general treatment of multivariate polynomials over multidimensional simplices is given by de Boor [30].

In what follows, multi-index notation denoted by the bold characters $\mathbf{i}$ and $\mathbf{j}$ is used. Multi-indices are n-tuples of nonnegative integers, the components of which start at zero; for instance, $\mathbf{i} = (i_1, i_2, \ldots, i_n)$. The norm of a multi-index $\mathbf{i}$, denoted by $|\mathbf{i}|$, is defined to be the sum of the components of $|\mathbf{i}|$, namely $|\mathbf{i}| = i_1 + i_2 + \cdots + i_n$ [28]. Let $\boldsymbol{\xi} = (\xi_1, \xi_2, \ldots, \xi_n)$, with the property $\sum_I \xi_I = 1$, be the barycentric coordinate of a simplex $\delta \in \mathbb{R}^{n-1}$. A Bernstein–Bézier surface of degree m over the simplex δ can be written in the form [30]

$$b(\boldsymbol{\xi}) = \sum_{|\mathbf{i}|=m} B_{\mathbf{i}}^m(\boldsymbol{\xi})b_{\mathbf{i}}, \tag{3.1}$$

where $b_{\mathbf{i}}$ is known as the Bézier ordinate associated with the control point $\mathbf{i}/m$. The control net of $b(\boldsymbol{\xi})$ is the network of $(n+1)$-dimensional points $(\mathbf{i}/m, b_{\mathbf{i}})$. In Eq. (3.1), $B_{\mathbf{i}}^m(\boldsymbol{\xi})$ are m-variate Bernstein polynomials in n variables. To elaborate, they are the terms in the multinomial expansion of unity, i.e.,

$$(\xi_1 + \xi_2 + \cdots + \xi_n)^m = \sum_{|\mathbf{i}|=m} B_{\mathbf{i}}^m(\boldsymbol{\xi}), \quad B_{\mathbf{i}}^m(\boldsymbol{\xi}) = \binom{m}{\mathbf{i}} \xi_1^{i_1} \xi_2^{i_2} \cdots \xi_n^{i_n}, \qquad (3.2)$$

where $\binom{m}{\mathbf{i}}$ is the multinomial coefficient, which is defined as

$$\binom{m}{\mathbf{i}} = \frac{m!}{i_1! i_2! \cdots i_n!}. \qquad (3.3)$$

In one dimension with $n = 2$, we have $\xi_1 = 1 - x$ and $\xi_2 = x$ as the barycentric coordinates of a simplex $\delta \in \mathbb{R}$. The univariate linear Bernstein polynomials $(m = 1)$ are $\{1 - x, x\}$; the quadratic polynomials $(m = 2)$ are $\{(1 - x)^2, 2(1 - x)x, x^2\}$; and the cubic polynomials $(m = 3)$ are $\{(1-x)^3, 3(1-x)^2x, 3(1-x)x^2, x^3\}$, where $x \in [0, 1]$. Multivariate Bernstein polynomials have properties very much like their univariate counterparts. From Eq. (3.2), some of the important properties of multivariate Bernstein polynomials, such as partition of unity, positivity, and cardinal interpolation, are easily inferred. The control points (circles) and associated Bézier ordinate values $(b_{\mathbf{i}})$ for a cubic Bernstein–Bézier triangular patch are shown in Fig. 2. The interested reader can refer to Böhm, Farin, and Kahmann [31], Farin [29], and Farin [28] for further details on the properties and applications of triangular Bernstein–Bézier patches.

Consider a point $\mathbf{x} \in \mathbb{R}^2$ that has n natural neighbors. Let the natural neighbor coordinates of $\mathbf{x}$ be $\boldsymbol{\Phi} = (\phi_1(\mathbf{x}), \phi_2(\mathbf{x}), \ldots, \phi_n(\mathbf{x}))$. Since $\sum_I \phi_I(\mathbf{x}) = 1$, we note that $\boldsymbol{\Phi}$ can be considered as a barycentric coordinate (nonunique) of the n-gon in the plane. The generalization of Bézier surfaces over a convex polygonal domain was proposed by Loop and DeRose [32]. By using $\boldsymbol{\Phi}$
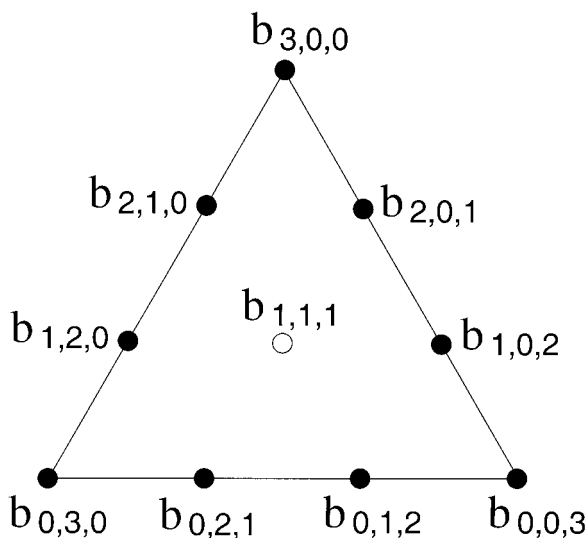

FIG. 2. Cubic Bernstein–Bézier triangular patch.

instead of $\boldsymbol{\xi}$ in Eq. (3.1), we can construct the surface [26]

$$w^m(\boldsymbol{\Phi}) = \sum_{|\mathbf{i}|=m} B_{\mathbf{i}}^m(\boldsymbol{\Phi}) b_{\mathbf{i}}. \qquad (3.4)$$

In the above equation, the Bézier ordinate $b_{\mathbf{i}}$ is associated with the control point $\mathbf{q_i} \in \mathbb{R}^2$, where $\mathbf{q_i}$ are the projection of the control points of the m-variate Bézier polynomial over the $(n-1)$-dimensional simplex onto the plane [26]:

$$\mathbf{q_i} = \sum_{|\mathbf{j}|=1} B_{\mathbf{j}}^1(\mathbf{i}/m) \mathbf{x_j}, \qquad |\mathbf{i}| = m. \qquad (3.5)$$

On the basis of Eq. (3.5), one can infer that the components of the barycentric coordinate $\boldsymbol{\xi}$ of the $(n-1)$-dimensional simplex is identical to that of the Sibson coordinate $\boldsymbol{\Phi}$ of the mapped n-gon on the plane.

The connectivity rule for Bézier simplexes states that the domain simplex has all vertices connected to all other vertices. If $\mathbf{q_i}$ and $\mathbf{q_j}$ are two Bézier points in the n-gon simplex, then the rule indicates that there must exist integers r and s such that the multi-indices $\mathbf{i}$ and $\mathbf{j}$ satisfy

$$\mathbf{i} - \mathbf{e}_r = \mathbf{j} - \mathbf{e}_s, \qquad (3.6)$$

where $\mathbf{e}_\alpha = (\delta_{1\alpha}, \delta_{2\alpha}, \ldots, \delta_{k\alpha}, \ldots, \delta_{n\alpha})$ denotes the multi-index having zero in all components except for the αth component, which is one. The projection of the control net of a cubic tetrahedron ($m = 3, n = 4$) onto the plane is shown in Fig. 3. In Fig. 3, the open circles are "boundary" control points, and the filled circles are center control points. The center control points are located at the centroid of the corresponding triangle; for instance, $\mathbf{q}_{1,1,1,0} = \frac{1}{3}(\mathbf{q}_{3,0,0,0} + \mathbf{q}_{0,3,0,0} + \mathbf{q}_{0,0,3,0})$.

If we choose $m = 1$ in Eq. (3.4) and let $w_I = w(\mathbf{x}_I)$ denote the nodal function value, we obtain

$$w^1(\mathbf{x}) = \sum_{I=1}^n \phi_1^{\delta_{1I}}(\mathbf{x}) \phi_2^{\delta_{2I}}(\mathbf{x}) \cdots \phi_n^{\delta_{nI}}(\mathbf{x}) b_{\mathbf{e}_I} = \sum_{I=1}^n \phi_I(\mathbf{x}) w_I, \qquad (3.7)$$
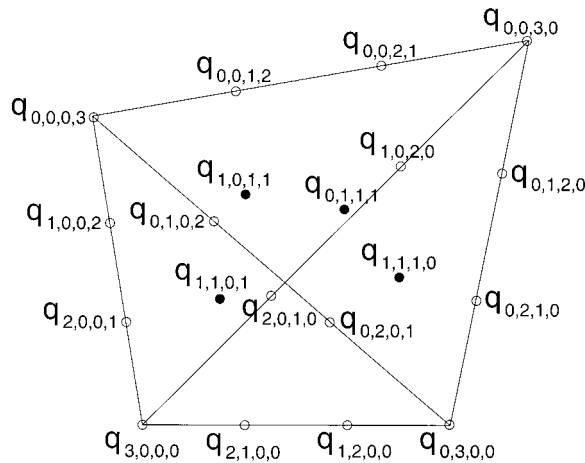

FIG. 3.   Projection of the control net of a cubic tetrahedron onto the plane [26].

which is the original Sibson interpolant. Hence, Eq. (3.4) can be viewed as a generalized form of the Sibson interpolant.

For $m = 3$, we arrive at the following surface representation [26]:

$$w^3(\mathbf{\Phi}) = \sum_{|\mathbf{i}|=3} B_{\mathbf{i}}^3(\mathbf{\Phi})b_{\mathbf{i}}, \tag{3.8}$$

which is the C^1 interpolant that we use in the natural element method.

A. Properties

Farin [26] has outlined the properties of the C^1 interpolant given in Eq. (3.8). Here we discuss some of the important properties that are germane to a Galerkin formulation that is pursued in this article.

1. Smoothness. Farin [26] has shown that the interpolant proposed in Eq. (3.8) is $C^1(\Omega)$. Consider an open bounded domain $\Omega \subset \mathbb{R}^2$. Let $\mathbf{x} \in \Omega$ be any point that has n natural neighbors, and $\mathbf{x}_I$ be the nodal coordinate of node I ($I = 1, n$). Sibson coordinates $\phi_I(\mathbf{x})$ are continuously differentiable at all points $\mathbf{x} \neq \mathbf{x}_I$. Since $B_{\mathbf{i}}^3$ in Eq. (3.8) is composed of products of $C^0(\Omega)$ natural neighbor shape functions raised to a power, it is evident that the new interpolant is also continuously differentiable at all points $\mathbf{x} \neq \mathbf{x}_I$. The "boundary" control points for the n-gon with respect to node I lie along the lines joining $\mathbf{x}_I$ and the remaining $n-1$ nodes. Let these $n-1$ directions be denoted by d_j ($j = 1, n-1$). The control points in the tangent plane with respect to node I are the ones that lie along d_j and are connected to the control point $\mathbf{q}_{3e_I}$ (node I)—see Eq. (3.6). Farin [26] noted that the directional derivative at $\mathbf{x}_I$ along an arbitrary direction d is a linear combination of the directional derivatives along the directions d_j. Moreover, since all the control points are coplanar, the directional derivative along d is also in the plane, and, hence, the differentiability at $\mathbf{x} = \mathbf{x}_I$ is met. By virtue of the above inferences, the $C^1(\Omega)$ continuity of the interpolant is established.

2. Quadratic Completeness. The $C^1(\Omega)$ interpolant has quadratic completeness, i.e., it can exactly reproduce a general quadratic function [26]. In keeping with finite element usage [33], we use the term completeness, which is better known as precision in approximation theory. As opposed to the above, the $C^1(\Omega)$ interpolant proposed by Sibson [34] can reproduce only spherical quadratics, i.e., functions of the form $a_0 + a_1x + a_2y + a_3(x^2 + y^2)$. By virtue of the quadratic completeness property, Farin's $C^1(\Omega)$ interpolant can exactly represent a state of constant curvature (second derivatives of the displacement for the thin plate problem), which is required to pass the patch test for a fourth-order PDE such as the biharmonic equation.

By judicious choice of the Bézier ordinates, Farin [35] realized a quadratic precision interpolant. For a cubic n-gon simplex in the plane, there are $n^2 + \binom{n}{3}$ control points, and, consequently, the same number of Bézier ordinates. Of these, n^2 control points lie along the lines joining nodes $\mathbf{x}_I$ and $\mathbf{x}_J$ ($I < J \leq n$), with four control points lying along any one such line. For instance, if $I = 1, J = 3$, and $n = 4$, the control points along the line joining $\mathbf{x}_1$ and $\mathbf{x}_3$ are $\mathbf{q}_{3,0,0,0}, \mathbf{q}_{2,0,1,0}, \mathbf{q}_{1,0,2,0}$, and $\mathbf{q}_{0,0,3,0}$. The associated "boundary" Bézier ordinates to these n^2 control points are of two distinct types, namely ordinates $b_{\mathbf{i}}$ whose subscript contains one 3 and all other zeros (for example, $b_{0,3,0,0}$), or ordinates $b_{\mathbf{i}}$ whose subscript have one 2, one 1, and all other zeros (for example, $b_{1,2,0,0}$). The former (nodal or vertex ordinates) are precisely equal to the nodal function value, and the latter Bézier ordinates are easily found in the tangent planes (see Section IV.B). The additional $\binom{n}{3}$ control points are associated with "free" Bézier ordinates $b_{\mathbf{i}}$

whose subscript contains three 1's and all other zeros (for example, $b_{1,1,1,0}$). The Bézier ordinates mentioned within braces are for $n = 4$; the control points for this case are indicated in Fig. 3. An optimal choice for the center Bézier ordinate is given by $b_{1,1,1,0} = \frac{3}{2}a - \frac{1}{2}c$ [35], where a is the centroid of the tangent Bézier ordinates and c is the centroid of the vertex (nodal) Bézier ordinates. The above choice of the center Bézier ordinate guarantees quadratic precision. An illustration of the evaluation of the Bézier ordinates for a cubic Bernstein–Bézier triangular patch is shown in Fig. 4. Referring to Fig. 4, we can express $b_{1,1,1}$ as [35, 26]

$$b_{1,1,1} = \frac{3}{2}\,a - \frac{1}{2}\,c, \tag{3.9a}$$

where

$$a = \frac{b_{2,1,0} + b_{1,2,0} + b_{2,0,1} + b_{1,0,2} + b_{0,2,1} + b_{0,1,2}}{6}, \; c = \frac{b_{3,0,0} + b_{0,3,0} + b_{0,0,3}}{3}. \tag{3.9b}$$

3. Univariate Interpolation. In one dimension, the $C^0(\Omega)$ natural element method is identical to linear finite elements [23]. We now consider the $C^1(\Omega)$ natural neighbor interpolant in one dimension. Let $\Omega = (0, 1) \subset \mathbb{R}$ be an open bounded domain. Any point $x \in \Omega$ has two natural neighbors, but a point $x \in \partial\Omega$ has only one neighbor. Let $x \in \Omega$ be a point that has two natural neighbors at $x = 0$ and $x = 1$. Then, Eq. (3.8) reduces to

$$w(\mathbf{\Phi}) = \sum_{i_1+i_2=3} \frac{3!}{i_1!i_2!}\; \phi_1^{i_1}(\mathbf{\Phi})\phi_2^{i_2}(\mathbf{\Phi})b_{i_1,i_2}. \tag{3.10}$$

Since $\phi_1 = 1 - x$ and $\phi_2 = x$ are the natural neighbor shape functions (barycentric coordinates) of the point x, we can expand the above equation to obtain

$$w(x) = (1 - x)^3 b_{3,0} + 3(1 - x)^2 x b_{2,1} + 3(1 - x)x^2 b_{1,2} + x^3 b_{0,3}, \tag{3.11}$$

which is a cubic polynomial curve between the two nodes. In the above equation, $b_{3,0} = w(0), b_{0,3} = w(1)$, and $b_{2,1}$ and $b_{1,2}$ are related to the function values and their derivatives at $x = 0$ and $x = 1$, respectively.

FIG. 4.   Evaluation of the Bézier ordinates for a cubic triangular surface patch [31].

4.   Cubic Polynomial along the Boundary $\partial\Omega$.   We assume that the discrete model consists of a set of nodes N that describes a convex domain $\Omega \subset \mathbb{R}^2$, with $\partial\Omega$ represented by the boundary of the convex hull CH(N). On the boundary of the convex hull, any point $\mathbf{x}$ has only two neighbors [26]. Consequently, by Eq. (3.11) in the previous subsection, we immediately arrive at the result that cubic interpolation is realized along the boundary of the convex hull.

5.   Bivariate Interpolation.   If a point $\mathbf{x} \in \Omega \subset \mathbb{R}^2$ has two natural neighbors ($n = 2$), the interpolant is cubic between the two nodes; if $n = 3$, the approximation is a cubic surface over a triangular patch; and if $n = 4$, the approximation is a bicubic patch [26].

B.   NEM Trial Function

We use the interpolant presented in Eq. (3.8) as the $C^1(\Omega)$ NEM trial function. Let the point $\mathbf{x} \in \Omega \subset \mathbb{R}^2$ have n natural neighbors, with $\phi_I(\mathbf{x})$ the natural neighbor shape function of node I ($I = 1, n$). Consider an interpolation scheme for a scalar-valued function $w(\mathbf{x}): \Omega \subset \mathbb{R}^2 \to \mathbb{R}$, in the form

$$w^h(\mathbf{\Phi}) = \sum_{|\mathbf{i}|=3} B_{\mathbf{i}}^3(\mathbf{\Phi})b_{\mathbf{i}}, \tag{3.12}$$

where the dependence on position $\mathbf{x}$ is implicit, since the components of $\mathbf{\Phi}$ are the natural neighbor shape functions that are functions of $\mathbf{x}$. We reiterate that there are $n^2 + \binom{n}{3}$ Bézier ordinates in Eq. (3.12), and, consequently, $n^2 + \binom{n}{3}$ terms on the right-hand side of the above equation.

   The above form of the interpolant is suitable for applications in the context of data interpolation or surface approximation, since nodal function values and sometimes even nodal gradient data are known *a priori*. For the numerical solution of PDEs by a Galerkin procedure, however, this is not the case, since nodal function and nodal gradient values are unknowns, which are to be determined from the solution of the discrete system: $\mathbf{Kd} = \mathbf{f}$. To meet the desired goal, we suggest a transformation that renders the resulting interpolant amenable to numerical computations and implementation in the context of the numerical solution of PDEs. This is achieved by recasting Eq. (3.12) in the following form (matrix notation):

$$w^h(\mathbf{\Phi}) = \{\mathbf{B}(\mathbf{\Phi})\}^T\{\mathbf{b}\} = \{\mathbf{B}(\mathbf{\Phi})\}^T[\mathbf{T}]\{\mathbf{w}\} = \{\mathbf{\Psi}(\mathbf{\Phi})\}^T\{\mathbf{w}\}, \tag{3.13a}$$

where

$$\{\mathbf{b}\} = [\mathbf{T}]\{\mathbf{w}\}, \quad \{\mathbf{\Psi}(\mathbf{\Phi})\}^T = \{\mathbf{B}(\mathbf{\Phi})\}^T[\mathbf{T}]. \tag{3.13b}$$

In Eq. (3.13), $\{\mathbf{B}\}$ and $\{\mathbf{b}\}$ are column vectors of dimension $n^2 + \binom{n}{3}$, and $[\mathbf{T}]$ is a transformation matrix of dimensions $(n^2 + \binom{n}{3}) \times 3n$. The transpose of the shape function vector $\{\mathbf{\Psi}(\mathbf{\Phi})\}^T = \{\psi_1(\mathbf{\Phi}), \psi_2(\mathbf{\Phi}), \psi_3(\mathbf{\Phi}), \ldots, \psi_{3n-2}(\mathbf{\Phi}), \psi_{3n-1}(\mathbf{\Phi}), \psi_{3n}(\mathbf{\Phi})\}$, and the transpose of the nodal vector $\{\mathbf{w}\}^T = \{w_1, \theta_{1x}, \theta_{1y}, \ldots, w_n, \theta_{nx}, \theta_{ny}\}$, where $w_I = w(\mathbf{x}_I)$ are the nodal function values, and $\theta_{Ix} = w_{,x}(\mathbf{x}_I)$ and $\theta_{Iy} = w_{,y}(\mathbf{x}_I)$ are the nodal gradient values. For the thin plate problem, w_I are the nodal displacements, and θ_{Ix} and θ_{Iy} are the nodal rotations. The matrix $[\mathbf{T}]$ is a transformation matrix that maps the nodal function and gradient values to the Bézier ordinates. The transformation from $\{\mathbf{B}(\mathbf{\Phi})\} \to \{\mathbf{\Psi}(\mathbf{\Phi})\}$ that we propose in Eq. (3.13b) is based on a simple observation. In order to construct a $C^1(\Omega)$ surface over an unstructured nodal grid, in general the nodal function values and nodal gradient values are required. In the Bernstein–Bézier surface representation given in Eq. (3.12), the vertex Bézier ordinates are identical to the nodal function values, and the tangent and center Bézier ordinates are related to the nodal gradient data. Hence, in its current form, the local interpolant is dependent on coefficients (Bézier ordinates) that

vary from point to point. The matrix $[\mathbf{T}]$ facilitates the representation of the interpolant in terms of nodal function values and nodal gradients, which renders it amenable to use in a PDE-setting; moreover, interpolation to both is realized (Section IV.C). In this light, we can view the C^1 NEM interpolant as a bivariate generalization of one-dimensional Hermite cubic polynomials. In one dimension, the equivalence of the NEM interpolant to cubic Hermite finite elements is shown in Section IV.B.

On constructing the transformation matrix $[\mathbf{T}]$ and carrying out the matrix-vector multiplication indicated in Eq. (3.13b), we can express the $C^1(\Omega)$ NEM trial function in standard shape function notation as

$$w^h(\mathbf{x}) = \sum_{j=1}^{3n} \psi_j(\mathbf{x}) w_j, \tag{3.14}$$

where $\psi_{3I-2}(\mathbf{x}), \psi_{3I-1}(\mathbf{x})$, and $\psi_{3I}(\mathbf{x})$ are the shape functions for node I that are associated with the nodal degrees of freedom w_I, θ_{Ix}, and θ_{Iy}, respectively.

1. Support of C^1 Shape Functions.   Consider node $I \in N$, where N is the set consisting of n natural neighbors for a point $\mathbf{x} \in \Omega \subset \mathbb{R}^2$. The $C^1(\Omega)$ shape functions associated with node I are $\psi_{3I-2}(\mathbf{x}), \psi_{3I-1}(\mathbf{x})$, and $\psi_{3I}(\mathbf{x})$. These shape functions are derived from a Bernstein–Bézier surface representation, in which the natural neighbor shape functions are used as barycentric coordinates of a point $\mathbf{x}$. Consequently, the $C^1(\Omega)$ shape functions retain the compact support properties of $\phi_I(\mathbf{x})$, and, hence, a local interpolant is realized. Akin to $\phi_I(\mathbf{x})$, the support of the shape functions $\psi_{3I-2}(\mathbf{x}), \psi_{3I-1}(\mathbf{x})$, and $\psi_{3I}(\mathbf{x})$ are the intersection of the convex hull CH(N) with the union of all Delaunay circumcircles that pass through node I [26]. Consider a unit square discretized by 25 (5×5) equi-spaced nodes [Fig. 5(a)]. The support for the shape functions $\phi_{3A-2}(\mathbf{x})$ and $\phi_{3A-1}(\mathbf{x})$ associated with node A are illustrated in Figs. 5(b) and 5(c), respectively.

IV. NUMERICAL COMPUTATION OF SHAPE FUNCTIONS

In this section, we first present the expressions for Bernstein–Bézier basis functions as a function of Sibson's coordinate $\mathbf{\Phi}$. Then, we describe in detail the construction of the transformation matrix $[\mathbf{T}]$ and the subsequent evaluation of NEM shape functions. Lastly, some key properties of the newly developed $C^1(\Omega)$ NEM shape functions $\mathbf{\Psi}(\mathbf{\Phi})$ are presented.

A. Bernstein–Bézier Basis Functions

Bernstein–Bézier (BB) basis functions are defined in Eq. (3.2). For a cubic n-gon simplex in Sibson's coordinates, we obtain

$$B_{\mathbf{i}}^3(\mathbf{\Phi}) = \binom{3}{\mathbf{i}} \phi_1^{i_1} \phi_2^{i_2} \cdots \phi_n^{i_n}, \tag{4.1}$$

where $\mathbf{i} = i_1 + i_2 + \cdots + i_n = 3$. For the cubic case, only three distinct types of basis functions arise, namely those corresponding to $\mathbf{i} = 3\mathbf{e}_I, \mathbf{i} = 2\mathbf{e}_I + \mathbf{e}_J$, and $\mathbf{i} = \mathbf{e}_I + \mathbf{e}_J + \mathbf{e}_K$. For convenience, we let $I \equiv 1, J \equiv 2$, and $K \equiv 3$. Then, the corresponding BB-basis functions are given by

$$B_{3,0,0}(\mathbf{x}) = \phi_1^3(\mathbf{x}), \quad B_{2,1,0}(\mathbf{x}) = 3\phi_1^2(\mathbf{x})\phi_2(\mathbf{x}), \quad B_{1,1,1}(\mathbf{x}) = 6\phi_1(\mathbf{x})\phi_2(\mathbf{x})\phi_3(\mathbf{x}). \tag{4.2}$$
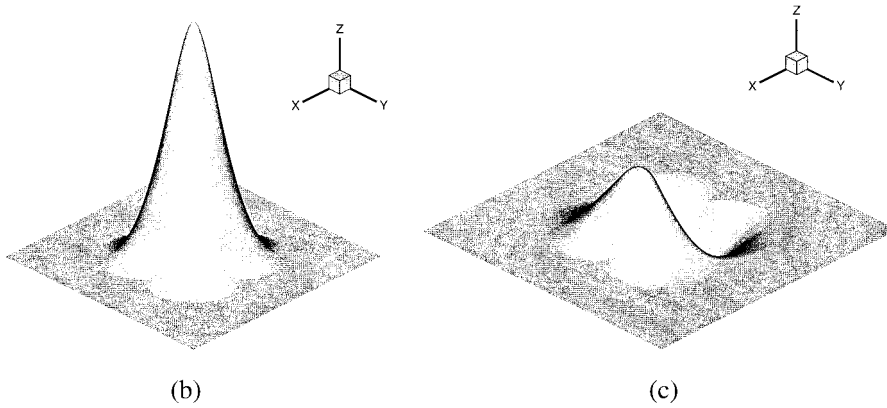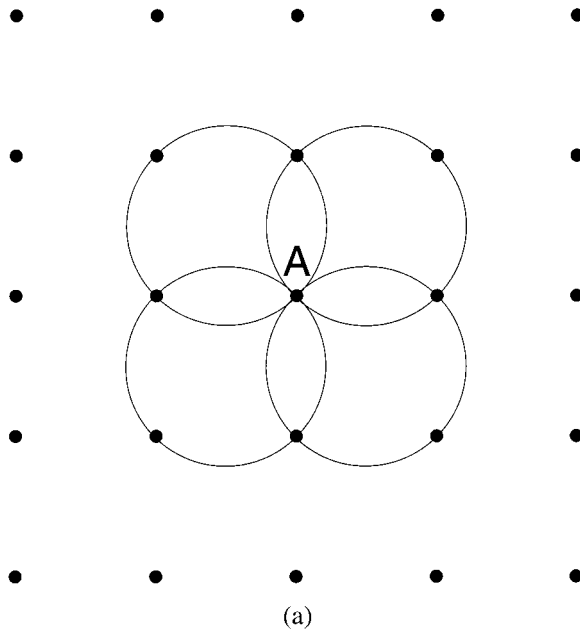
(a)

(b)   (c)

FIG. 5. Support for $C^1(\Omega)$ NEM shape function: (a) nodal grid; (b) shape function $\psi_{3A-2}(\mathbf{x})$; and (c) shape function $\psi_{3A-1}(\mathbf{x})$.

By definition, the three basis functions can be represented in the form

$$B_{i_1,i_2,i_3}(\mathbf{x}) = \frac{3!}{i_1!i_2!i_3!}\, \phi_1^{i_1}(\mathbf{x})\phi_2^{i_2}(\mathbf{x})\phi_3^{i_3}(\mathbf{x}), \tag{4.3}$$

where the choices $(3,0,0), (2,1,0)$, and $(1,1,1)$ for the 3-tuple (i_1, i_2, i_3) lead to the equations indicated in Eq. (4.2). The first derivatives of $B_{i_1,i_2,i_3}(\mathbf{x})$ can now be written as

$$\frac{\partial B_{i_1,i_2,i_3}(\mathbf{x})}{\partial \alpha} = B_{i_1,i_2,i_3}(\mathbf{x})C_{i_1,i_2,i_3}(\mathbf{x}),$$

$$C_{i_1,i_2,i_3}(\mathbf{x}) = \sum_{k=1}^{3} i_k\, \frac{\phi_{k,\alpha}(\mathbf{x})}{\phi_k(\mathbf{x})}, \qquad (\alpha = x, y), \tag{4.4}$$

and its second derivatives are given by

$$\frac{\partial^2 B_{i_1,i_2,i_3}(\mathbf{x})}{\partial\alpha\partial\beta} = \frac{\partial B_{i_1,i_2,i_3}(\mathbf{x})}{\partial\beta} C_{i_1,i_2,i_3}(\mathbf{x}) + B_{i_1,i_2,i_3}(\mathbf{x}) \frac{\partial C_{i_1,i_2,i_3}(\mathbf{x})}{\partial\beta}, \qquad (4.5a)$$

where

$$\frac{\partial C_{i_1,i_2,i_3}(\mathbf{x})}{\partial\beta} = \sum_{k=1}^{3} i_k \frac{\phi_k(\mathbf{x})\phi_{k,\alpha\beta}(\mathbf{x}) - \phi_{k,\alpha}(\mathbf{x})\phi_{k,\beta}(\mathbf{x})}{\phi_k^2(\mathbf{x})}, \qquad (\alpha,\beta = x, y). \quad (4.5b)$$

From the viewpoint of theoretical exposition, the above expressions for the Bernstein–Bézier basis function derivatives are compact and appealing. Nevertheless, in the numerical implementation, the derivatives of the basis functions given in Eq. (4.2) are explicitly computed. By this approach, simplifications arise and one can group like terms together, which leads to fewer arithmetic operations in the computations.

B. Construction of the Transformation Matrix [T]

As can be inferred from Section III.B, the construction of the transformation matrix $[\mathbf{T}]$ is the key step in transforming the Bernstein–Bézier representation of the trial function to the shape function form given in Eq. (3.14). Since this is central to the computational methodology that is adopted here, a detailed description of its formation is shown below.

We first present the relations between Bézier ordinates and the nodal function and gradient values, and then proceed to outline the structure and computational algorithm to construct the transformation matrix $[\mathbf{T}]$. The nodal or vertex Bézier ordinates are equal to the nodal function values, i.e.,

$$b_{\mathbf{i}} = w_I, \qquad \mathbf{i} = 3\mathbf{e}_I \tag{4.6}$$

for the Bézier ordinate at node I. The tangent Bézier ordinates are related to the nodal function and nodal gradient values. Let d be the direction along the line $\mathbf{x}_I$ to $\mathbf{x}_J$ and $\hat{d}$ be that from $\mathbf{x}_J$ to $\mathbf{x}_I$. The directional derivative of the function $w(\mathbf{x})$ along the directions d and $\hat{d}$ are given by

$$\frac{\partial w(\mathbf{x})}{\partial d} = \nabla w(\mathbf{x}) \cdot \mathbf{d} = \frac{\partial w(\mathbf{x})}{\partial x} d_x^{IJ} + \frac{\partial w(\mathbf{x})}{\partial y} d_y^{IJ}, \tag{4.7a}$$

$$\frac{\partial w(\mathbf{x})}{\partial \hat{d}} = \nabla w(\mathbf{x}) \cdot \hat{\mathbf{d}} = -\left(\frac{\partial w(\mathbf{x})}{\partial x} d_x^{IJ} + \frac{\partial w(\mathbf{x})}{\partial y} d_y^{IJ} \right), \tag{4.7b}$$

where $\hat{\mathbf{d}} = -\mathbf{d}$, and $d_x^{IJ} = x_J - x_I$ and $d_y^{IJ} = y_J - y_I$ are the Cartesian components of the vector $\mathbf{d}$. The directional derivative at $\mathbf{x}_I$ along d and the directional derivative at $\mathbf{x}_J$ along $\hat{d}$ can be expressed as

$$\frac{\partial w(\mathbf{x}_I)}{\partial d} = \theta_{Ix} d_x^{IJ} + \theta_{Iy} d_y^{IJ}, \tag{4.8a}$$

$$\frac{\partial w(\mathbf{x}_J)}{\partial \hat{d}} = -(\theta_{Jx} d_x^{IJ} + \theta_{Jy} d_y^{IJ}). \tag{4.8b}$$

The tangent Bézier ordinates that lie in the tangent plane are determined through the relations [28]

$$\frac{\partial w(\mathbf{x}_I)}{\partial d} = 3(b_{\mathbf{i}} - b_{\mathbf{j}}), \qquad \mathbf{i} = 2\mathbf{e}_I + \mathbf{e}_J, \qquad \mathbf{j} = 3\mathbf{e}_I, \tag{4.9a}$$

$$\frac{\partial w(\mathbf{x}_J)}{\partial \hat{d}} = 3(b_{\mathbf{i}} - b_{\mathbf{j}}), \quad \mathbf{i} = \mathbf{e}_I + 2\mathbf{e}_J, \quad \mathbf{j} = 3\mathbf{e}_J, \tag{4.9b}$$

which on using Eqs. (4.6) and (4.8) and rearranging terms results in the following expressions for the tangent Bézier ordinates:

$$b_{2\mathbf{e}_I + \mathbf{e}_J} = \frac{1}{3} \left(\theta_{I_x} d_x^{IJ} + \theta_{I_y} d_y^{IJ} \right) + w_I, \tag{4.10a}$$

$$b_{\mathbf{e}_I + 2\mathbf{e}_J} = -\frac{1}{3} \left(\theta_{J_x} d_x^{IJ} + \theta_{J_y} d_y^{IJ} \right) + w_J. \tag{4.10b}$$

Now, the center Bézier ordinates are computed using Eq. (3.9). Consider the center ordinate $b_{\mathbf{i}}$ with subscript $\mathbf{i} = \mathbf{e}_I + \mathbf{e}_J + \mathbf{e}_K$, i.e., the corresponding control point lies at the centroid of triangle $(\mathbf{x}_I, \mathbf{x}_J, \mathbf{x}_K)$. Hence, on using Eqs. (4.6) and (4.10) in conjunction with Eq. (3.9), we obtain the following expression for the center ordinate:

$$b_{\mathbf{i}} = \frac{w_I + w_J + w_K}{3} + \frac{\alpha_I \theta_{Ix} + \beta_I \theta_{Iy} + \alpha_J \theta_{Jx} + \beta_J \theta_{Jy} + \alpha_K \theta_{Kx} + \beta_K \theta_{Ky}}{4}, \tag{4.11a}$$

$$\mathbf{i} = \mathbf{e}_I + \mathbf{e}_J + \mathbf{e}_K, \tag{4.11b}$$

where

$$\alpha_I = \frac{d_x^{IJ} + d_x^{IK}}{3}, \quad \alpha_J = \frac{-d_x^{IJ} + d_x^{JK}}{3}, \quad \alpha_K = \frac{-d_x^{IK} - d_x^{JK}}{3}, \tag{4.12a}$$

$$\beta_I = \frac{d_y^{IJ} + d_y^{IK}}{3}, \quad \beta_J = \frac{-d_y^{IJ} + d_y^{JK}}{3}, \quad \beta_K = \frac{-d_y^{IK} - d_y^{JK}}{3}, \tag{4.12b}$$

$$d_x^{IJ} = x_J - x_I, \quad d_x^{JK} = x_K - x_I, \quad d_x^{JK} = x_K - x_J, \tag{4.12c}$$

$$d_y^{IJ} = y_J - y_I, \quad d_y^{IK} = y_K - y_I, \quad d_y^{JK} = y_K - y_J. \tag{4.12d}$$

The storage structure for the transformation matrix $[\mathbf{T}]$ is shown in Fig. 6, and a pseudo-code for its construction is presented in Table I. The map from the nodal function values to the vertex
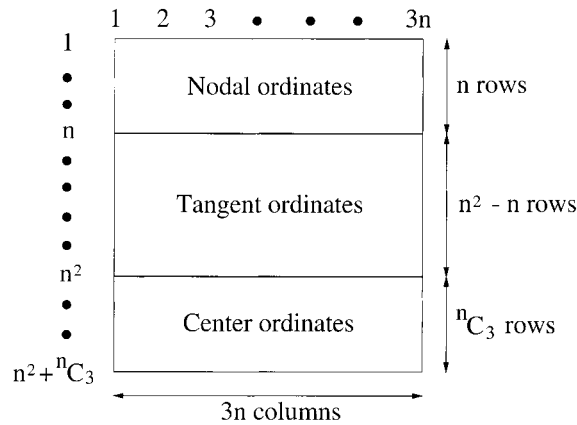

FIG. 6. Storage structure for the transformation matrix $[\mathbf{T}]$.

TABLE I.   Pseudo-code for construction of the transformation matrix $[\mathbf{T}]$.

1. Initialize matrix $[\mathbf{T}] = 0$;
2. Initialize matrix $[\mathbf{R}] = 0$;
3. for $I = 1 \rightarrow n$ {
    - $T(I, 3I - 2) = 1$;
  }
4. row $= n$;
5. for $I = 1 \rightarrow n - 1$ {
    (a) for $J = I + 1 \rightarrow n$ {
        - row $\leftarrow$ row $+ 1$;
        - $T(\text{row}, 3I - 2) = 1; T(\text{row}, 3I - 1) = d_x^{IJ}/3; T(\text{row}, 3I) = d_y^{IJ}/3$;
        - $R(I, J) = $ row;
        - row $\leftarrow$ row $+ 1$;
        - $T(\text{row}, 3I - 2) = 1; T(\text{row}, 3I - 1) = -d_x^{IJ}/3; T(\text{row}, 3I) = -d_y^{IJ}/3$;
        - $R(J, I) = $ row;
      }
  }
6. row $= n^2$;
7. for $I = 1 \rightarrow n - 2$ {
    (a) for $J = I + 1 \rightarrow n - 1$ {
        i. for $K = J + 1 \rightarrow n$ {
            - row $\leftarrow$ row $+ 1$;
            - compute $\alpha_I, \alpha_J, \alpha_K, \beta_I, \beta_J, \beta_K$ using Eq. (4.12);
            - $T(\text{row}, 3I - 2) = 1/3; T(\text{row}, 3I - 1) = \alpha_I/4; T(\text{row}, 3I) = \beta_I/4$;
            - $T(\text{row}, 3J - 2) = 1/3; T(\text{row}, 3J - 1) = \alpha_J/4; T(\text{row}, J) = \beta_J/4$;
            - $T(\text{row}, 3K - 2) = 1/3; T(\text{row}, 3K - 1) = \alpha_K/4$;
            - $T(\text{row}, 3K) = \beta_K/4$;
          }
      }
  }

Bézier ordinates is stored in the first n rows; the next $n^2 - n$ rows pertain to the tangent Bézier ordinates; and the last block of $\binom{n}{3}$ rows relate the nodal function and gradient values to the center Bézier ordinates. In Fig. 7, the vertex, tangent, and center Bézier ordinates with respect to node 1 are indicated for a pentagonal simplex ($n = 5$). An outline of the algorithm presented in Table I follows. The matrix $[\mathbf{T}]$ as well as an $n \times n$ matrix $[\mathbf{R}]$ are initialized to zero. The matrix $[\mathbf{R}]$ stores the row number of the contribution in $[\mathbf{T}]$ due to the tangent Bézier ordinates. For the first block of n rows, Eq. (4.6) is invoked so as to set the Ith row and $(3I - 2)$-column position in $[\mathbf{T}]$ to unity. In the second block (tangent ordinates), the entries in $[\mathbf{T}]$ are evaluated using Eq. (4.10). The loops are executed such that for any node I ($1 \leq I \leq n - 1$), the entries for all tangent ordinates along the line joining $\mathbf{x}_I$ to $\mathbf{x}_J$ ($I < J \leq n$) are computed. In Fig. 7, the filled square corresponds to the Bézier ordinate given by Eq. (4.10a), and the open square corresponds to that given by Eq. (4.10b). Lastly, the entries in the matrix $[\mathbf{T}]$ due to the center ordinates (see filled ellipses in Fig. 7) are stored. This involves the 3-tuple (I, J, K) such that $1 \leq I \leq n - 2, I < J \leq n - 1$, and $J < K \leq n$. Here, the entries in $[\mathbf{T}]$ are computed using Eqs. (4.11) and (4.12). Both $[\mathbf{T}]$ as well as $[\mathbf{R}]$ are required to evaluate the parameters that appear in Eq. (4.12). In addition to storing the entries in $[\mathbf{T}]$, the BB-basis functions and its derivatives given in Section IV.A are also computed within each block. Once the construction of the transformation matrix $[\mathbf{T}]$ is complete,
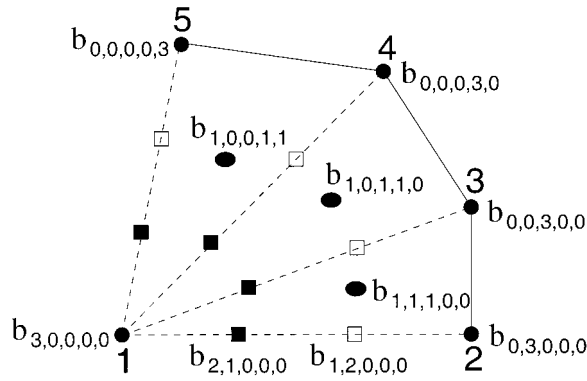
FIG. 7. Bézier ordinates used in the algorithm for a pentagonal simplex.

a matrix-vector product is carried out to compute the shape functions $\psi_j(\mathbf{x})$ and their derivatives $\psi_{j,\alpha}(\mathbf{x})$ and $\psi_{j,\alpha\beta}(\mathbf{x})$ $(\alpha, \beta = x, y)$:

$$\{\boldsymbol{\Psi}(\boldsymbol{\Phi})\}^T = \{\mathbf{B}(\boldsymbol{\Phi})\}^T[\mathbf{T}], \tag{4.13a}$$

$$\{\boldsymbol{\Psi}_{,\alpha}(\boldsymbol{\Phi})\}^T = \{\mathbf{B}_{,\alpha}(\boldsymbol{\Phi})\}^T[\mathbf{T}], \tag{4.13b}$$

$$\{\boldsymbol{\Psi}_{,\alpha\beta}(\boldsymbol{\Phi})\}^T = \{\mathbf{B}_{,\alpha\beta}(\boldsymbol{\Phi})\}^T[\mathbf{T}]. \tag{4.13c}$$

In order to illustrate the shape function computations, we present two examples. First, in one dimension, it is shown that the matrix $[\mathbf{T}]$ transforms cubic Bernstein polynomials to cubic Hermite polynomials that are used in higher-order finite elements. Then, the transformation matrix $[\mathbf{T}]$ for a cubic triangular patch $(n = 3)$ is presented to illustrate the computational methodology for shape function calculations.

Example 1. Consider a point $x \in \Omega = (0, 1)$ with natural neighbors at $x_1 = 0$ and $x_2 = 1$. We recall Eq. (3.11), which is the one-dimensional $C^1(\Omega)$ interpolant in BB-form:

$$w(x) = B_{3,0}^3 b_{3,0} + B_{2,1}^3 b_{2,1} + B_{1,2}^3 b_{1,2} + B_{0,3}^3 b_{0,3}, \tag{4.14a}$$

where

$$B_{3,0}^3 = (1 - x)^3, \quad B_{2,1}^3 = 3(1 - x)^2 x, \quad B_{1,2}^3 = 3(1 - x)x^2, \quad B_{0,3}^3 = x^3. \tag{4.14b}$$

From Eq. (4.6), we immediately have $w_1 = b_{3,0}$ and $w_2 = b_{0,3}$. Let $\theta_1 = w_{,x}(x_1)$ and $\theta_2 = w_{,x}(x_2)$. Then, on using Eq. (4.10), we obtain

$$b_{2,1} = \frac{\theta_1}{3} + w_1, \tag{4.15a}$$

$$b_{1,2} = -\frac{\theta_2}{3} + w_2, \tag{4.15b}$$

and, hence, the transformation equation given in Eq. (3.13b) can be written as

$$\left\{ \begin{array}{c} b_{3,0} \\ b_{0,3} \\ b_{2,1} \\ b_{1,2} \end{array} \right\} = \left[\begin{array}{cccc} 1 & 0 & 0 & 0 \\ 0 & 0 & 1 & 0 \\ 1 & \frac{1}{3} & 0 & 0 \\ 0 & 0 & 1 & -\frac{1}{3} \end{array} \right] \left\{ \begin{array}{c} w_1 \\ \theta_1 \\ w_2 \\ \theta_2 \end{array} \right\}. \tag{4.16}$$

On using Eq. (4.13a) in conjunction with Eqs. (4.14) and (4.16), we obtain the following equations for the $C^1(\Omega)$ NEM shape functions:

$$\psi_1(x) = B_{3,0}^3 + B_{2,1}^3 = 1 - 3x^2 + 2x^3, \tag{4.17a}$$

$$\psi_2(x) = \frac{1}{3} B_{2,1}^3 = x - 2x^2 + x^3, \tag{4.17b}$$

$$\psi_3(x) = B_{0,3}^3 + B_{1,2}^3 = 3x^2 - 2x^3, \tag{4.17c}$$

$$\psi_4(x) = -\frac{1}{3} B_{1,2}^3 = -x^2 + x^3, \tag{4.17d}$$

which are cubic Hermite polynomials.

Example 2. The Bézier ordinates for a cubic triangular patch $(m = 3, n = 3)$ are indicated in Fig. 4 and the relation for the center ordinate is presented in Eq. (3.9). For any point $\mathbf{x}$ in a triangle, the natural neighbor shape functions $\phi_I(\mathbf{x})$ at $\mathbf{x}$ are identical to the barycentric coordinates of $\mathbf{x}$ [26]. For simplicity, we consider the Δ_{ABC} with vertices $A(0,0)$, $B(1,0)$, and $C(0,1)$. There are ten cubic triangular Bézier ordinates, of which three are vertex ordinates, six are tangent ordinates, and one is a center ("free") ordinate. On using Eqs. (4.10) and (4.11), with the parameters computed from Eq. (4.12), we can relate the nodal vector $\{\mathbf{w}\}$ to the Bézier ordinate vector $\{\mathbf{b}\}$ through the following equation:

$$\{\mathbf{b}\} = [\mathbf{T}]\{\mathbf{w}\} \Rightarrow \begin{Bmatrix} b_{3,0,0} \\ b_{0,3,0} \\ b_{0,0,3} \\ b_{2,1,0} \\ b_{1,2,0} \\ b_{2,0,1} \\ b_{1,0,2} \\ b_{0,2,1} \\ b_{0,1,2} \\ b_{1,1,1} \end{Bmatrix} = \begin{bmatrix} 1 & 0 & 0 & 0 & 0 & 0 & 0 & 0 & 0 \\ 0 & 0 & 0 & 1 & 0 & 0 & 0 & 0 & 0 \\ 0 & 0 & 0 & 0 & 0 & 0 & 1 & 0 & 0 \\ 1 & \frac{1}{3} & 0 & 0 & 0 & 0 & 0 & 0 & 0 \\ 0 & 0 & 0 & 1 & -\frac{1}{3} & 0 & 0 & 0 & 0 \\ 1 & 0 & \frac{1}{3} & 0 & 0 & 0 & 0 & 0 & 0 \\ 0 & 0 & 0 & 0 & 0 & 0 & 1 & 0 & -\frac{1}{3} \\ 0 & 0 & 0 & 1 & -\frac{1}{3} & \frac{1}{3} & 0 & 0 & 0 \\ 0 & 0 & 0 & 0 & 0 & 0 & 1 & \frac{1}{3} & -\frac{1}{3} \\ \frac{1}{3} & \frac{1}{12} & \frac{1}{12} & \frac{1}{3} & -\frac{1}{6} & \frac{1}{12} & \frac{1}{3} & \frac{1}{12} & -\frac{1}{6} \end{bmatrix} \begin{Bmatrix} w_1 \\ \theta_{1x} \\ \theta_{1y} \\ w_2 \\ \theta_{2x} \\ \theta_{2y} \\ w_3 \\ \theta_{3x} \\ \theta_{3y} \end{Bmatrix}. \tag{4.18}$$

Let the nodes be numbered as $1, 2,$ and 3. Then, the BB-basis functions are

$$B_{i_1,i_2,i_3}(\mathbf{x}) = \frac{3!}{i_1! i_2! i_3!} \phi_1^{i_1}(\mathbf{x}) \phi_2^{i_2}(\mathbf{x}) \phi_3^{i_3}(\mathbf{x}), \tag{4.19}$$

where $i_1 + i_2 + i_3 = 3$ and $\phi_1(\mathbf{x}) = 1 - x - y$, $\phi_2(\mathbf{x}) = x$, and $\phi_3(\mathbf{x}) = y$ are the natural neighbor shape functions. The ten components of the vector $\{\mathbf{B}(\boldsymbol{\Phi})\}$ are computed from the above equation. Since $[\mathbf{T}]$ is known from Eq. (4.18), the shape function vector $\{\boldsymbol{\Psi}(\boldsymbol{\Phi})\}$ and its derivatives are readily computed from Eq. (4.13).

Remark. *A cubic Bernstein–Bézier surface representation over a triangle leads to a C^0 interpolant. In the natural element method, as a point $\mathbf{x}$ approaches a Delaunay edge, which is within the convex hull of the domain, the number of neighbors for $\mathbf{x}$ is greater than three, and consequently a smooth interpolant is realized in that region.*

C. Properties

Most of the properties of $C^0(\Omega)$ natural neighbor shape functions and Bernstein–Bézier basis functions are retained by $C^1(\Omega)$ shape functions, but there do exist a few differences and some

notable exceptions. We present some of the most important properties of $C^1(\Omega)$ NEM shape functions.

1. Interpolation, Partition of Unity, and Quadratic Completeness. The interpolant proposed in Eq. (3.14) is an alternate representation of Farin's $C^1(\Omega)$ interpolant that appears in Eq. (3.12). Since $C^1(\Omega)$ NEM shape functions are linear combinations of Bernstein–Bézier basis functions, cardinal interpolation of the function $w(\mathbf{x})$ is immediately seen:

$$\psi_{3I-2}(\mathbf{x}_J) = \delta_{IJ}, \qquad \psi_{3I-1}(\mathbf{x}_J) = 0, \qquad \psi_{3I}(\mathbf{x}_J) = 0 \Rightarrow w^h(\mathbf{x}_J) = w(\mathbf{x}_J). \quad (4.20)$$

In addition, it is obvious that the quadratic precision property of Eq. (3.12) also holds for the recast form proposed in Eq. (3.14). By the above inferences, we immediately arrive at the following properties:

$$\sum_{j=1}^{3n} \psi_j(\mathbf{x})w_j = w(\mathbf{x}_j) \quad \forall\, w(\mathbf{x}) = \sum_{\substack{i+j \leq 2 \\ i,j \geq 0}} a_{ij}x^i y^j, \qquad a_{ij} \in \mathbb{R}, \tag{4.21a}$$

$$\sum_{I=1}^{n} \psi_{3I-2}(\mathbf{x}) = 1. \tag{4.21b}$$

Equation (4.21a) is the statement of quadratic completeness of the NEM interpolant, and Eq. (4.21b), which can be viewed as a consequence of Eq. (4.21a) for $w(\mathbf{x}) \equiv 1$, indicates that the NEM shape functions associated with the nodal function values form a partition of unity.

2. Positivity. Natural neighbor shape functions $\phi_I(\mathbf{x})$ as well as Bernstein–Bézier basis functions $B_{\mathbf{i}}^3$ share the property of positivity:

$$0 \leq \phi_I(\mathbf{x}) \leq 1, \qquad 0 \leq B_{\mathbf{i}}^3 \leq 1. \tag{4.22}$$

As opposed to the above, only the NEM shape functions $\psi_{3I-2}(\mathbf{x})$ that correspond to the nodal function values share the above property, namely

$$0 \leq \psi_{3I-2}(\mathbf{x}) \leq 1, \tag{4.23}$$

whereas $\psi_{3I-1}(\mathbf{x})$ as well as $\psi_{3I}(\mathbf{x})$ can assume both positive as well as negative values. A shape function of the form $\psi_{3I-2}(\mathbf{x})$ is illustrated in Fig. 5(b), and one akin to $\psi_{3I-1}(\mathbf{x})$ is shown in Fig. 5(c).

3. Interpolation to Nodal Rotations. It was mentioned in Section IV.B that the NEM interpolant in Eq. (3.14) interpolates to nodal function and nodal gradient values. The former is evident by virtue of Eq. (4.20). The latter is shown below.

Claim. *The $C^1(\Omega)$ interpolant in Eq. (3.14) interpolates to nodal gradient values*:

$$w_{,x}^h(\mathbf{x}_I) = \theta_{Ix}, \qquad w_{,y}^h(\mathbf{x}_I) = \theta_{Iy}. \tag{4.24}$$

Proof. Consider a cubic n-gon simplex in the plane, where n is the number of natural neighbors for a point $\mathbf{x} \in \Omega$. The Bézier ordinate at $\mathbf{x}_I$ is $b_{3\mathbf{e}_I}$, and the directional derivative along a direction d at $\mathbf{x}_I$ is influenced only by the tangent Bézier ordinates that are connected to $b_{3\mathbf{e}_I}$. These ordinates are of the form $b_{2\mathbf{e}_I+\mathbf{e}_J}$, where $J = I$ is a vertex ordinate, and the rest are tangent ordinates. It is evident that the Bézier ordinates $b_{2\mathbf{e}_I+\mathbf{e}_J}$ are related to only w_I, θ_{Ix}, and θ_{Iy}—see Eq. (4.10).

The Bernstein–Bézier basis function derivatives associated with these ordinates are the only ones that are nonzero at $\mathbf{x}_I$. For simplicity, without any loss of generality, we let $I = 1$, i.e., local node 1 with nodal location $\mathbf{x}_1$ is considered. In Fig. 2, where $n = 3$, the ordinates of interest are $b_{3,0,0}, b_{2,1,0}$, and $b_{2,0,1}$, and in Fig. 3, where $n = 4$, the ordinates are $b_{3,0,0,0}, b_{2,1,0,0}, b_{2,0,1,0}$, and $b_{2,0,0,1}$. Hence, the vector consisting of Bernstein–Bézier basis function derivatives at the point $\mathbf{x}_1$ can be written as

$$\{\mathbf{B}_{,\alpha}(\mathbf{x}_1)\}^T = \left\{ B_{1,\alpha}(\mathbf{x}_1), \underbrace{\ldots\ldots}_{n-1\ \text{zeros}}, \underbrace{B_{2,\alpha}(\mathbf{x}_1), 0, \ldots, B_{n,\alpha}(\mathbf{x}_1), 0}_{[(n^2-n)/2]\text{zeros}}, \underbrace{\ldots\ldots}_{\binom{n}{3}\ \text{zeros}} \right\}, \qquad (4.25a)$$

where

$$B_1(\mathbf{x}) = \phi_1^3(\mathbf{x}), \qquad B_J(\mathbf{x}) = 3\phi_1^2(\mathbf{x})\phi_J(\mathbf{x}), \qquad (J = 2, \ldots, n), \qquad (4.25b)$$

$$B_{J,\alpha}(\mathbf{x}_1) = 3\phi_{J,\alpha}(\mathbf{x}_1), \qquad (J = 1, 2, \ldots, n; \alpha = x, y), \qquad (4.25c)$$

where the interpolating property $\phi_J(\mathbf{x}_1) = \delta_{J1}$ is used to arrive at Eq. (4.25c). Now, we consider the structure of $[\mathbf{T}]$ to determine the entries that are of interest. Since the Bézier ordinates $b_{2\mathbf{e}_1+\mathbf{e}_J}$ are related to only w_1, θ_{1x}, and θ_{1y}, it suffices if we only consider the first three columns of $[\mathbf{T}]$. Let $[\hat{\mathbf{T}}]$ be such a submatrix of $[\mathbf{T}]$. We must point out that the entries in $[\hat{\mathbf{T}}]$ due to the center Bézier ordinates are nonzero. The associated basis function derivatives are zero, however, and, hence, the center ordinates provide no contribution to any of the components in the NEM shape function vector. Using Eq. (4.10), the matrix $[\hat{\mathbf{T}}]$ can be written as

$$[\hat{\mathbf{T}}] = \begin{bmatrix} \begin{array}{|ccc|} \hline 1 & 0 & 0 \\ 0 & 0 & 0 \\ \cdots & \cdots & \cdots \\ 0 & 0 & 0 \\ \hline 1 & \alpha_x^{12} & \alpha_y^{12} \\ 0 & 0 & 0 \\ 1 & \alpha_x^{13} & \alpha_y^{13} \\ 0 & 0 & 0 \\ \cdots & \cdots & \cdots \\ \cdots & \cdots & \cdots \\ 1 & \alpha_x^{1n} & \alpha_y^{1n} \\ 0 & 0 & 0 \\ \hline c_{11} & c_{12} & c_{13} \\ \cdots & \cdots & \cdots \\ c_{m1} & c_{m2} & c_{m3} \\ \hline \end{array} \end{bmatrix}, \qquad (4.26)$$

where $c_{ij} \in \mathbb{R}, m = \binom{n}{3}$, and $\alpha_x^{1J} = d_x^{1J}/3$ and $\alpha_y^{1J} = d_y^{1J}/3$. The submatrices corresponding to the vertex, tangent, and center Bézier ordinates are indicated by the enclosed boxes in the above equation. By virtue of Eq. (4.12), we have

$$d_x^{1J} = x_J - x_1, \qquad d_y^{1J} = y_J - y_1, \qquad (J = 2, 3, \ldots, n). \qquad (4.27)$$

On taking the product of Eqs. (4.25) and (4.26), we can write the nonzero $C^1(\Omega)$ shape function derivatives as

$$\psi_{1,\alpha}(\mathbf{x}_1) = \sum_{J=1}^{n} \phi_{J,\alpha}(\mathbf{x}_1), \qquad\qquad (4.28a)$$

$$\psi_{2,\alpha}(\mathbf{x}_1) = \sum_{J=2}^{n} \phi_{J,\alpha}(\mathbf{x}_1)d_x^{1J}, \qquad\qquad (4.28b)$$

$$\psi_{3,\alpha}(\mathbf{x}_1) = \sum_{J=2}^{n} \phi_{J,\alpha}(\mathbf{x}_1)d_y^{1J}. \qquad\qquad (4.28c)$$

Since $\sum_J \phi_J(\mathbf{x}_1) = 1$, it follows that Eq. (4.28a) is identically equal to zero. On substituting Eq. (4.27) in the above equation and noting that $\phi_{1,\alpha}(\mathbf{x}_1) = -\sum_{J=2}^{n} \phi_{J,\alpha}(\mathbf{x}_1)$, we obtain

$$\psi_{1,\alpha}(\mathbf{x}_1) = 0, \qquad\qquad (4.29a)$$

$$\psi_{2,\alpha}(\mathbf{x}_1) = \sum_{J=1}^{n} \phi_{J,\alpha}(\mathbf{x}_1)x_J, \qquad\qquad (4.29b)$$

$$\psi_{3,\alpha}(\mathbf{x}_1) = \sum_{J=1}^{n} \phi_{J,\alpha}(\mathbf{x}_1)y_J. \qquad\qquad (4.29c)$$

But the natural neighbor shape functions satisfy the local coordinate property given in Eq. (2.4), namely

$$\sum_{J=1}^{n} \phi_J(\mathbf{x})\mathbf{x}_J = \mathbf{x}, \qquad\qquad (4.30)$$

and, hence, on taking the derivative of the above equation with respect to x and y in succession and substituting in Eq. (4.29), we obtain

$$\psi_{1,x}(\mathbf{x}_1) = 0, \qquad \psi_{2,x}(\mathbf{x}_1) = 1, \qquad \psi_{3,x}(\mathbf{x}_1) = 0, \qquad\qquad (4.31a)$$

$$\psi_{1,y}(\mathbf{x}_1) = 0, \qquad \psi_{2,y}(\mathbf{x}_1) = 0, \qquad \psi_{3,y}(\mathbf{x}_1) = 1. \qquad\qquad (4.31b)$$

Now, the derivatives of the NEM trial function given in Eq. (3.14) can be written as

$$w_{,x}^h(\mathbf{x}_1) = \psi_{1,x}(\mathbf{x}_1)w_1 + \psi_{2,x}(\mathbf{x}_1)\theta_{1x} + \psi_{3,x}(\mathbf{x}_1)\theta_{1y}, \qquad\qquad (4.32a)$$

$$w_{,y}^h(\mathbf{x}_1) = \psi_{1,y}(\mathbf{x}_1)w_1 + \psi_{2,y}(\mathbf{x}_1)\theta_{1x} + \psi_{3,y}(\mathbf{x}_1)\theta_{1y}, \qquad\qquad (4.32b)$$

and, hence, on using Eq. (4.31) in the above equation, we obtain

$$w_{,x}^h(\mathbf{x}_1) = \theta_{1x}, \qquad w_{,y}^h(\mathbf{x}_1) = \theta_{1y}. \qquad\qquad (4.33)$$

Since the choice $I = 1$ is arbitrary, the above relations are readily extended for all I $(1 \leq I \leq n)$, which leads us to the desired result:

$$w_{,x}^h(\mathbf{x}_I) = \theta_{Ix}, \qquad w_{,y}^h(\mathbf{x}_I) = \theta_{Iy}. \qquad\qquad (4.34) \quad \blacksquare$$

By virtue of Eqs. (4.20) and (4.31), we note an additional property—$C^1(\Omega)$ NEM shape functions are cardinal with respect to function evaluation, as well as differentiation with respect to the coordinate directions:

$$\psi_{3I-2}(\mathbf{x}_J) = \delta_{IJ}, \qquad \psi_{3I-1}(\mathbf{x}_J) = 0, \qquad \psi_{3I}(\mathbf{x}_J) = 0, \tag{4.35a}$$

$$\psi_{3I-2,x}(\mathbf{x}_J) = 0, \qquad \psi_{3I-1,x}(\mathbf{x}_J) = \delta_{IJ}, \qquad \psi_{3I,x}(\mathbf{x}_J) = 0, \tag{4.35b}$$

$$\psi_{3I-2,y}(\mathbf{x}_J) = 0, \qquad \psi_{3I-1,y}(\mathbf{x}_J) = 0, \qquad \psi_{3I,y}(\mathbf{x}_J) = \delta_{IJ}. \tag{4.35c}$$

V. GOVERNING EQUATIONS AND WEAK FORM

As a model fourth-order partial differential equation, we consider the biharmonic equation with Dirichlet boundary conditions, which is described as

$$\Delta^2 w = f \quad \text{in } \Omega, \tag{5.1a}$$

$$w = g_1 \quad \text{on } \Gamma, \tag{5.1b}$$

$$\frac{\partial w}{\partial n} = g_2 \quad \text{on } \Gamma, \tag{5.1c}$$

where $\Omega \subset \mathbb{R}^2$ is an open bounded domain and Γ is its boundary, n is the outward normal to Ω, and Δ is the Laplacian operator. The weak or variational problem is posed as:

Find $w \in V = H^2(\Omega)$ such that $a(w, v) = (f, v) \quad \forall v \in V_0 = H_0^2(\Omega)$, \qquad (5.2)

where $a(w, v): V \times V \to \mathbb{R}$ is the bilinear form for the biharmonic operator and the $L^2(\Omega)$ inner product on the right-hand side is defined as

$$(f, v) = \int_\Omega fv \, d\Omega. \tag{5.3}$$

In Eq. (5.2), V is the Sobolev space of functions with square-integrable second derivatives in Ω, and the Sobolev space $V_0 = \{v \in H^2(\Omega), v = 0, \partial v/\partial n = 0 \text{ on } \Gamma\}$. As opposed to the Laplace operator, two distinct Dirichlet (bilinear) forms exist for the biharmonic operator [36]:

$$a_1(w, v) = \int_\Omega \Delta w \Delta v \, d\Omega, \tag{5.4a}$$

$$a_2(w, v) = \int_\Omega \left[(w_{,xx} - w_{,yy})(v_{,xx} - v_{,yy}) + 4w_{,xy}v_{,xy} \right] d\Omega. \tag{5.4b}$$

Any linear combination of the above two equations is also a Dirichlet form. For the plate problem, the bilinear form (strain energy) is given by [37, 38]:

$$a_3(w, v) = \int_\Omega \left[\Delta w \Delta v - (1 - \nu)(w_{,xx}v_{,yy} + w_{,yy}v_{,xx} - 2w_{,xy}v_{,xy}) \right] d\Omega, \tag{5.5}$$

where ν is the Poisson's ratio. By virtue of Green's theorem, we have

$$\int_\Omega \Delta w \Delta v \, d\Omega = \int_\Omega \Delta^2 w v \, d\Omega - \int_\Gamma \Delta w_{,n} v \, d\Gamma - \int_\Gamma \Delta w v_{,n} \, d\Gamma, \tag{5.6a}$$

$$\int_\Omega [w_{,xx}v_{,yy} + w_{,yy}v_{,xx} - 2w_{,xy}v_{,xy}]\, d\Omega = \int_\Gamma w_{,tt}v_{,n}\, d\Gamma - \int_\Gamma w_{,nt}v_{,t}\, d\Gamma, \quad (5.6b)$$

where n and t are the outward normal and tangential directions to Γ. For the Dirichlet problem with $v \in V_0$, the boundary integrals in the above equations are zero, and w satisfies the strong form given in Eq. (5.1). The bilinear form for the biharmonic equation given in Eq. (5.4a) and that for the plate problem indicated in Eq. (5.5) are both bounded, symmetric, and positive definite operators in V_0, and, therefore, there exists a unique solution w to the variational problem in Eq. (5.2) [38].

Consider the Galerkin implementation for the natural element method. Using the bilinear form given in Eq. (5.4a), the weak form for the discrete problem can be stated as:

$$\text{Find } w \in V^h \subset V \text{ such that } a_1(w^h, v^h) = (f, v^h) \quad \forall\, v^h \in V_0^h \subset V_0. \quad (5.7)$$

In a Bubnov–Galerkin procedure, the trial function w^h as well as the test function v^h are represented in terms of the same shape functions. The trial and test functions are

$$\{w^h \quad v^h\} = \sum_{I=1}^n \{\Psi_I\}[\mathbf{w}_I \quad \mathbf{v}_I], \quad (5.8a)$$

where

$$\Psi_I^T = \left\{ \begin{array}{c} \psi_{3I-2} \\ \psi_{3I-1} \\ \psi_{3I} \end{array} \right\}, \qquad \mathbf{w}_I = \left\{ \begin{array}{c} w_I^h \\ \theta_{Ix}^{w^h} \\ \theta_{Iy}^{w^h} \end{array} \right\}, \qquad \mathbf{v}_I = \left\{ \begin{array}{c} v_I^h \\ \theta_{Ix}^{v^h} \\ \theta_{Iy}^{v^h} \end{array} \right\}. \quad (5.8b)$$

The discrete Laplacian for the trial and test functions can be written as

$$\{\Delta w^h \quad \Delta v^h\} = \sum_{I=1}^n \{\mathbf{B}_I\}[\mathbf{w}_I \quad \mathbf{v}_I], \quad (5.9a)$$

where

$$\mathbf{B}_I^T = \left\{ \begin{array}{c} \psi_{3I-2,xx} + \psi_{3I-2,yy} \\ \psi_{3I-1,xx} + \psi_{3I-1,yy} \\ \psi_{3I,xx} + \psi_{3I,yy} \end{array} \right\}. \quad (5.9b)$$

On substituting the trial and test functions in Eq. (5.7) and using the arbitrariness of nodal variations, the following discrete system of linear equations is obtained:

$$\mathbf{Kd} = \mathbf{f}, \quad (5.10)$$

where

$$\mathbf{K}_{IJ} = \int_{\Omega^h} \mathbf{B}_I^T \mathbf{B}_J\, d\Omega, \quad (5.11a)$$

$$\mathbf{f}_I = \int_{\Omega^h} \Psi_I^T f\, d\Omega. \quad (5.11b)$$

In the above equations, $\mathbf{d}$ is the vector of nodal function and gradient values, Ψ_I is the nodal shape function vector, and $\mathbf{B}_I$ is the discrete Laplacian vector.

VI. NUMERICAL RESULTS

The application of NEM to the biharmonic equation with Dirichlet boundary conditions is presented. The $L^2(\Omega)$ and energy error norms that are used in the analyses are defined as

$$\|w - w^h\|_{L^2(\Omega)} = \left(\int_\Omega (w - w^h)^2 \, d\Omega \right)^{1/2}, \qquad (6.1a)$$

$$\|w - w^h\|_{E(\Omega)} = \left(\frac{1}{2} \int_\Omega a_1(w - w^h, w - w^h) \, d\Omega \right)^{1/2}, \qquad (6.1b)$$

where w and w^h are the exact and numerical (NEM) solutions, respectively. Numerical integration of the weak form is carried out using symmetric quadrature rules for a triangle [39]. In the error norm computations, 25 point quadrature rule is used in each triangle. The packages *Triangle* [40] and *Show Me* [41] are used to construct and display the nodal discretization and Delaunay triangles.

A. Airy Stress Function

The Airy stress function in small displacement linear elastostatics satisfies the biharmonic equation. A wide range of two- and three-dimensional problems, ranging from homogeneous deformation to those with point and line singularities, are encompassed within this theoretical framework. In fracture mechanics, numerical methods are an invaluable tool to compute fracture parameters that are associated with the fracture and failure of cracked-bodies. Bernal and Whiteman [42] used finite difference approximations, and Gregory et al. [43] used local mesh refinement with modified C^1 bicubic interpolants to solve the two-dimensional biharmonic problem of an edge-cracked plate under uniaxial tension.

Let w be the Airy stress function in two-dimensional elasticity. As a benchmark problem (patch test) for the homogeneous biharmonic operator, we consider a circular plate under a biaxial state of stress:

$$\Delta^2 w = 0 \quad \text{in } \Omega, \qquad (6.2a)$$

$$w = a^2 \quad \text{on } \Gamma, \qquad (6.2b)$$

$$\frac{\partial w}{\partial r} = 2a \quad \text{on } \Gamma, \qquad (6.2c)$$

where $\Omega = \{(x, y) : x^2 + y^2 < a^2\}$ is a circular domain of radius a and Γ is its boundary.

In polar coordinates, the exact solution for the Airy stress function is: $w(r) = r^2$. Consider a circular domain of unit radius ($a = 1$); due to symmetry, only one-quarter of the circular domain is modeled with appropriate symmetry boundary conditions. The $L^2(\Omega)$ and energy error norm results for four quasi-regular nodal grids are presented in Table II. The nodal grid and the associated Delaunay triangles for a typical discretization are shown in Fig. 8. The nodal grids are constructed by setting a $L \times L \times L$ sub-division for the three boundaries. The case $L = 6$ is shown in Fig. 8, and the other grids correspond to $L = 12, 24$, and 48. In Fig. 9, the plot of w and $\partial w / \partial r$ vs. the radial distance r for the $L = 6$ grid is presented. In the computations, 25 equidistant output points between $r = 0$ and $r = 1$ are considered. Since the $C^1(\Omega)$ NEM interpolant has quadratic completeness, the numerical solution should be accurate within machine precision, which is 10^{-16} in double-precision arithmetic on a HP9000/s700 workstation. The inaccuracy in

TABLE II.   Relative error norms for the Airy stress function problem.

Nodal grids	Quadrature	$\dfrac{\|w-w^h\|_{L^2(\Omega)}}{\|w\|_{L^2(\Omega)}}$	$\dfrac{\|w-w^h\|_{E(\Omega)}}{\|w\|_{E(\Omega)}}$
	3	7.2×10^{-3}	2.7×10^{-1}
37	25	8.3×10^{-3}	1.1×10^{-1}
	37	9.7×10^{-3}	1.2×10^{-1}
	3	8.2×10^{-3}	2.3×10^{-1}
127	25	2.6×10^{-3}	9.6×10^{-2}
	37	3.6×10^{-3}	9.5×10^{-2}
	3	6.9×10^{-3}	2.0×10^{-1}
469	25	9.9×10^{-4}	7.3×10^{-2}
	37	1.6×10^{-3}	7.3×10^{-2}
	3	4.0×10^{-3}	1.5×10^{-1}
1801	25	4.7×10^{-4}	5.5×10^{-2}
	37	6.2×10^{-4}	5.3×10^{-2}

the NEM solution is due to numerical quadrature errors in the integration of the weak form, which was also observed for the patch test in two-dimensional elastostatics [23]. First and foremost, the numerical integration errors stem from the fact that the support of the shape functions do not coincide with the Delaunay triangles. In addition, the entries in the stiffness matrix $\mathbf{K}$ consist of products of second-order derivatives of NEM shape functions. The integrand is a rational function, which is not exactly integrated using polynomial-precision symmetric quadrature rules over triangles. The selection of an appropriate numerical quadrature scheme for NEM, however, is still an open issue.

B. Clamped Circular Plate

Consider the axi-symmetric problem of a clamped circular plate under a uniform transverse unit load ($f = 1$). The governing equations are:

$$\Delta^2 w = 1 \quad \text{in } \Omega, \tag{6.3a}$$

$$w = \frac{\partial w}{\partial r} = 0 \quad \text{on } \Gamma, \tag{6.3b}$$

where $\Omega = \{(x, y): x^2 + y^2 < a^2\}$ is a circular domain of radius a and Γ is its boundary. The exact solution to the above problem is given by [44]:

$$w(r) = \frac{1}{64} (a^2 - r^2)^2. \tag{6.4}$$

Consider a circular domain of unit radius; due to symmetry, only one-quarter of the circular domain is modeled. The nodal discretizations used in the analyses are: 37 [A], 127 [B], 271 [C], 469 [D], 721 [E], 1027 [F], 1387 [G], and 1801 [H] nodes. The subdivision for these grids are: $L = 6, 12, 18, 24, 30, 36, 42$, and 48. The discrete Kirchhoff element (DKT) is one of the most efficient and reliable finite elements for thin plate analysis [45]. In the DKT element, only C^0 continuity requirements are needed to be satisfied, with the Kirchhoff hypothesis being met at discrete points along the edges of the element. In Table III, the normalized center displacement for the above grids are presented, and in Fig. 10, the NEM results are illustrated. There is good
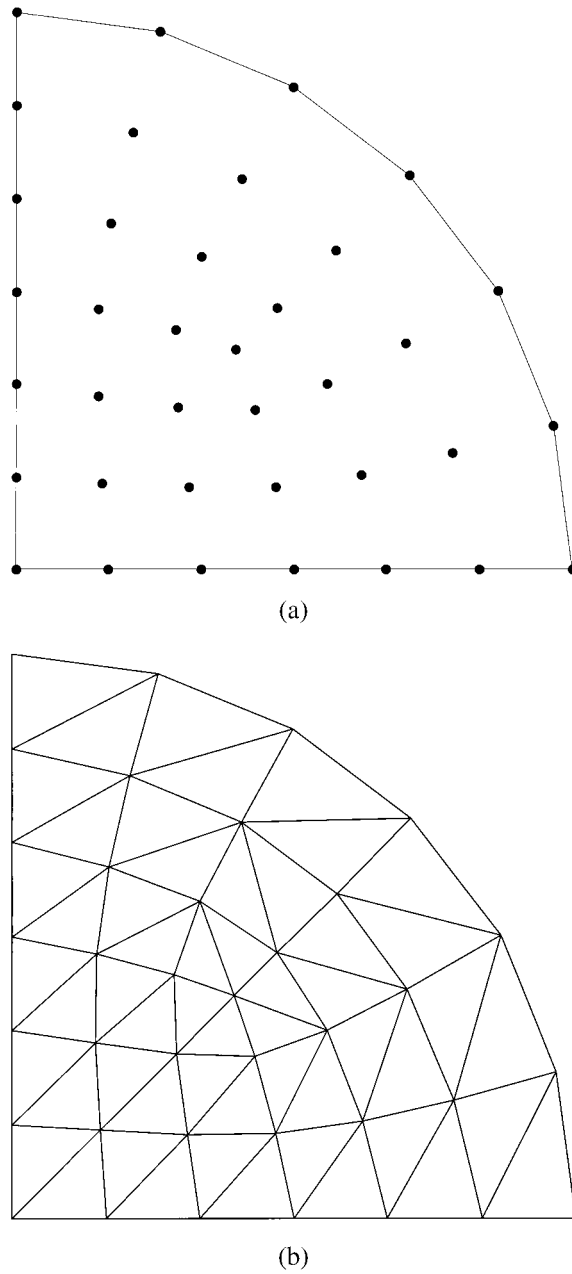
(a)

(b)

FIG. 8.   Quarter circular plate: (a) nodal discretization (37 nodes); and (b) Delaunay triangulation.

agreement between the NEM and exact solution. The convergence to the center displacement is monotonic, and the error in the center displacement is less than 2% for a grid with more than 200 nodes. A plot of w and $w_{,r}$ as a function of r is illustrated in Fig. 11. The grid shown in Fig. 8 is used, and 25 equi-spaced output points between $r = 0$ and $r = 1$ are chosen in the computations.
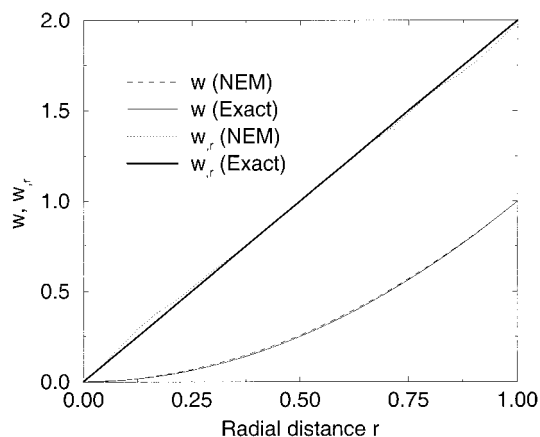
FIG. 9.   Plot of w and $w_{,r}$ vs. r for the Airy stress function problem (37 nodes).

A convergence study is carried out using the nodal grids A–H. The relative $L^2(\Omega)$ and energy error norms are shown against a measure of the nodal spacing h $(h = a/L, a = 1$ is the plate radius$)$ on a log–log plot (Fig. 12). In Fig. 12, the convergence rate is indicated by the value of R. The rate of convergence in displacement and energy is 0.95 and 0.41, respectively; optimal rates are 2 and 1 in displacement and energy for a conforming finite element with quadratic completeness [3]. In order to study the suboptimal rates of convergence, an eigenanalysis is carried out in the following section. The results indicate that the discrete bilinear operator is V_0^h-elliptic and, hence, stable, while the approximating space is poorly conditioned. The suboptimal rates of convergence are attributable to the latter factor in conjunction with the numerical integration errors in the computations.

C. Eigenanalysis

To study stability, we look at the properties of the approximating spaces and the ellipticity of the discrete bilinear operator. The EISPACK eigensolver package [46] is used to solve the eigenproblems that follow.

TABLE III.   Normalized center displacement for the uniformly loaded circular plate.

Nodal grids	$\frac{w_{NEM}^h}{w}$		$\frac{w_{DKT}^h}{w}$
	Quad = 3	Quad = 25	
37	1.0986	1.0408	1.0087
127	1.0817	1.0224	1.0026
271	1.0639	1.0147	1.0012
469	1.0565	1.0117	1.0007
721	1.0463	1.0095	1.0005
1027	1.0392	1.0082	1.0003
1387	1.0331	1.0071	1.0002
1801	1.0292	1.0061	1.0002

1. Linear Independence of Shape Functions.   The approximating space is studied by considering the linear independence of the shape functions [3]. To this end, we consider the following discrete eigenvalue problem:

$$\mathbf{M}\hat{\mathbf{d}} = \lambda^h \hat{\mathbf{d}}, \tag{6.5}$$

where $\hat{\mathbf{d}}$ and λ^h are the eigenvectors and eigenvalues of $\mathbf{M}$, and $\mathbf{M}$ is the mass matrix, which is given by

$$\mathbf{M}_{IJ} = \int_\Omega \mathbf{\Psi}_I^T \mathbf{\Psi}_J \, d\Omega. \tag{6.6}$$

The conditions number $\kappa(\mathbf{M}) = \lambda_{\max}(\mathbf{M})/\lambda_{\min}(\mathbf{M})$ is used as a measure of the linear independence of the shape functions. If the shape functions were orthonormal, $\mathbf{M}_{IJ}$ would be the identity matrix and $\kappa = 1$. The leading eigenvalue λ_{3I-2}^h, which corresponds to the eigenvector $\hat{\mathbf{d}}_{3I-2}$ is used to compute the condition number; the other eigenvalues are deemed spurious and vanish in the limit $h \to 0$ [3]. In Table IV, the condition number is computed for the nodal grids A, B, C, D, and H (see Section VI.B). It is seen that the condition numbers increase markedly with nodal refinement thereby indicating that the system is poorly conditioned. This indicates that the $C^1(\Omega)$ NEM approximation spaces are not uniformly linearly independent. An immediate consequence of this is that the accuracy of the computed results could be affected, since, if the condition number is 10^s, then as many as s digits may be lost during the solution of the system $\mathbf{Kd} = \mathbf{f}$ [3]. Keeping this in mind, we now consider the stability of the discrete operator, which is of far greater significance for the stability and convergence of the numerical method.

2. Ellipticity.   The continuity of the discrete bilinear operator $a(w^h, v^h): V^h \times V_0^h \to \mathbb{R}$ is established by virtue of choosing conforming finite-dimensional subspaces $w^h \in V^h$ and $v^h \in V_0^h$. For showing V_0^h-ellipticity of the operator, it suffices if the following condition is satisfied:

$$a(v^h, v^h) \geq \alpha \|v^h\|^2 \quad \forall \, v^h \in V_0^h \subset H_0^2(\Omega), \tag{6.7}$$

where the positive constant α is bounded away from zero. The ellipticity constant for the discrete operator is numerically estimated by considering the generalized eigenproblem associated with
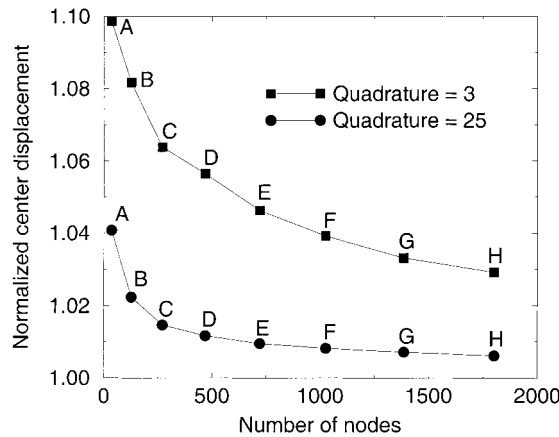

FIG. 10.   Variation of normalized center displacement with number of nodes for the uniformly loaded clamped circular plate.
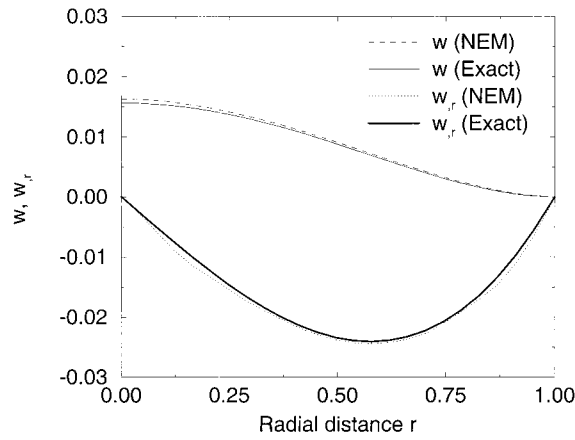
FIG. 11.   Plot of w and $w_{,r}$ vs. r for the uniformly loaded clamped circular plate (37 nodes).

the biharmonic equation:

$$\Delta^2 \tilde{w} = \lambda \tilde{w} \quad \text{in } \Omega, \tag{6.8a}$$

$$\tilde{w} = \tilde{w}_{,n} = 0 \quad \text{on } \Gamma, \tag{6.8b}$$

where $\tilde{w}$ is the natural mode of vibration of the plate, $\lambda = \omega^2$ is the eigenvalue, and ω the natural frequency of vibration. The equivalent variational form for the eigenproblem is:

$$\text{Find } \tilde{w} \in V = H^2(\Omega) \text{ such that } \int_\Omega \Delta \tilde{w} \Delta \tilde{v} \, d\Omega = \lambda(\tilde{w}, \tilde{v}) \quad \forall \tilde{v} \in V_0 = H_0^2(\Omega). \tag{6.9}$$

The weak form for the discrete problem is posed as:

$$\text{Find } \tilde{w}^h \in V^h \subset V \text{ such that } \int_\Omega \Delta \tilde{w}^h \Delta \tilde{v}^h \, d\Omega = \lambda^h(\tilde{w}^h, \tilde{v}^h) \quad \forall \tilde{v}^h \in V_0^h \subset V_0. \tag{6.10}$$
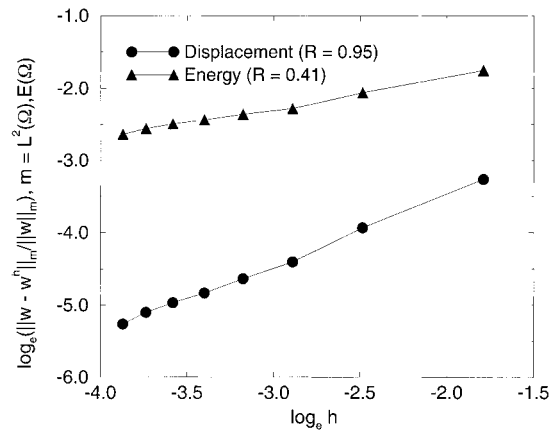

FIG. 12.   Rate of convergence in displacement and energy for the uniformly loaded clamped circular plate.

TABLE IV.   Condition number of the mass matrix.

Nodal grids	$\kappa = \frac{\lambda_{max}^h}{\lambda_{min}^h}$
37	8.57×10^3
127	8.35×10^4
271	2.69×10^5
469	5.87×10^5
1801	9.42×10^9

By substituting the discrete trial and test functions in the above equation and using the arbitrariness of nodal variations, we obtain the following discrete eigensystem:

$$\mathbf{K}\bar{\mathbf{d}} = \lambda^h \mathbf{M}\bar{\mathbf{d}}, \tag{6.11}$$

where $\bar{\mathbf{d}}$ and λ^h are the natural eigenmodes and eigenvalues, respectively, $\mathbf{K}_{IJ}$ is the nodal stiffness matrix that is defined in Eq. (5.11), and $\mathbf{M}_{IJ}$ is the mass matrix given in Eq. (6.6). For the symmetric bilinear form in Eq. (6.10) there exists an increasing sequence of strictly positive eigenvalues for the eigenproblem. By considering the Rayleigh quotient $R(v^h) = a(v^h, v^h)/(v^h, v^h)$ for the discrete problem in conjunction with Eqs. (6.11) and (6.7), we obtain the following result for the ellipticity constant:

$$\alpha = \inf\{R(v^h): v^h \in V_0^h\} = \lambda_1^h, \tag{6.12}$$

where λ_1^h is the lowest eigenvalue with $\omega_1^h = \sqrt{\lambda_1^h}$ the corresponding fundamental frequency. The fundamental frequency that corresponds to the lowest eigenvalue is computed for the nodal grids A–D. The reference solution for the fundamental frequency is $\omega_1 = 10.21$ [47]. The results for the normalized fundamental frequency are presented in Table V; there is good agreement between the numerical solution (NEM) and the reference solution. Clearly, $\alpha = (\omega_1^h)^2$ is approximately a constant and is bounded away from zero. This implies that the ellipticity condition given in Eq. (6.7) is satisfied, and, hence, the discrete bilinear operator is stable.

VII. CONCLUSIONS

Natural neighbor coordinates were proposed by Sibson [20] as a means for data interpolation and smoothing. In a previous study [23], its potential as a paradigm for the solution of second-order elliptic PDEs was demonstrated. Natural neighbor coordinates have optimum spatial adjacency, and provide a natural means to assign weights to irregularly spaced nodal data; it is envisaged that this could be of merit in the development of lumped mass schemes for wave propagation in elastodynamics and electromagnetics. In this article, a C^1 natural element method was presented, and its

TABLE V.   Normalized fundamental frequency for the clamped circular plate.

Nodal grids	$\frac{\omega_1^h}{\omega_1}$
37	0.9854
127	0.9927
271	0.9951
469	0.9962

application to the biharmonic equation, a fourth-order elliptic partial differential equation (PDE), was carried out. Farin [26] has developed a C^1 interpolant by embedding Sibson's coordinate [20] in the Bernstein–Bézier surface representation of a cubic simplex. The C^1 NEM interpolant that we propose is constructed by a suitable transformation of Bernstein basis functions that appear in Farin's C^1 interpolant. This transformation results in the representation of the interpolant in terms of nodal function and nodal gradient values, which renders it amenable to use in a Galerkin scheme for the solution of PDEs. The C^1 interpolant has quadratic completeness, interpolates to nodal function and nodal gradient values, and reduces to a cubic polynomial on the boundary of the domain. In one dimension, C^1 NEM interpolation is identical to cubic Hermite finite elements. In the application to the biharmonic equation, a standard Galerkin procedure was used to obtain the discrete equations. In the patch test for the biharmonic operator, issues pertaining to the accurate numerical integration of the weak form were raised. Excellent agreement with the exact solution for the uniformly loaded clamped circular plate was obtained, and convergence to the exact center displacement was monotonic with nodal refinement.

Issues pertaining to stability were probed by carrying out an eigenanalysis. Numerical results show that the mass matrix is poorly conditioned. The satisfaction of the ellipticity condition was met, with the ellipticity constant α being the square of the fundamental frequency of the clamped plate. This established the stability of the discrete biharmonic operator. The NEM results for the fundamental frequency matched the reference solution for the clamped plate problem. In this context, a potential application of the C^1 interpolant is in the numerical computation of natural modes and frequencies of plates.

The computational costs of the C^1 natural element method are more than its C^0 variant. The increased costs are primarily due to the fact that three degrees of freedom are associated with each node; the C^1 shape function computations involve basic linear algebra matrix-vector operations and the costs are not significantly more than that incurred in the evaluation of C^0 natural neighbor shape functions.

The computational methodology presented here demonstrates an effective, accurate, and appealing choice to construct a C^1 conforming method for the solution of fourth-order elliptic PDEs.

References

1. Y. A. Chu and B. Moran, A computational model for nucleation of solid–solid phase transformations, Mod Simul Mater Sci Eng 3 (1995), 455–471.

2. R. Clough and J. L. Tocher, ''Finite element stiffness matrices for analysis of plates in bending,'' Proc 1st Conf Matrix Meth Struct Mech, Wright–Patterson AFB, 1965.

3. G. Strang and G. Fix, An analysis of the finite element method, Prentice–Hall, Englewood Cliffs, N.J., 1973.

4. P. Alfeld, A bivariate C^2 Clough–Tocher scheme, Comp Aided Geom Des 1 (1984), 257–267.

5. G. Farin, A modified Clough–Tocher interpolant, Comp Aided Geom Des 2 (1985), 19–27.

6. C. de Veubeke, A conforming finite element for plate bending, Int J Solids Struct 4 (1968), 95–108.

7. B. Irons, A conforming quartic triangular element for plate bending, Int J Numer Meth Eng 1 (1969), 29–45.

8. K. Bell, A refined triangular plate bending finite element, Int J Numer Meth Eng 1 (1969), 101–122.

9. M. J. Powell and M. A. Sabin, Piecewise quadratic approximations on triangles, ACM Trans Math Soft 3 (1977), 316–325.

10. A. Peano, Conforming approximations for Kirchhoff plates and shells, Int J Numer Meth Eng 14 (1979), 1273–1291.

11. M. J. Lai and P. Wenston, Report on numerical experiments with bivariate C^1 cubic splines for numerical solution of partial differential equations. Tech Rep, Dept Math, Univ Georgia, 1998.

12. D. Shepard, A two-dimensional interpolation function for irregularly spaced points, ACM Nat Conf 1968, pp. 517–524.

13. H. Wendland, Piecewise polynomial, positive definite and compactly supported radial basis functions of minimal degree, Adv Comp Math 4 (1995), 389–396.

14. P. Lancaster and K. Salkauskas, Surfaces generated by moving least squares methods, Math Comp 37 (1981), 141–158.

15. H. Wendland, Meshless Galerkin approximation using radial basis functions, Math Comp, to appear.

16. G. E. Fasshauer, Solving differential equations with radial basis functions: Multilevel methods and smoothing, Adv Comp Math, to appear.

17. P. Hein, Diffuse element method applied to Kirchhoff plates. Tech Report, Dept Civil Eng, Northwestern Univ, 1993.

18. P. Krysl and T. Belytschko, Analysis of thin plates by the element-free Galerkin method, Comp Mech 17 (1996), 26–35.

19. B. Donning, Meshless methods for shear-deformable beams and plates. Master's thesis, Northwestern Univ, 1997.

20. R. Sibson, A vector identity for the Dirichlet tesselation, Math Proc Cambridge Phil Soc 87 (1980), 151–155.

21. L. Traversoni, Natural neighbor finite elements, Int Conf Hydraul Eng Soft Hydrosoft Proc, Vol 2, 1994 pp. 291–297. Computational Mechanics Publications.

22. J. Braun and M. Sambridge, A numerical method for solving partial differential equations on highly irregular evolving grids, Nature 376 (1995), 655–660.

23. N. Sukumar, B. Moran, and T. Belytschko, The natural element method in solid mechanics, Int J Numer Meth Eng 43 (1998), 839–887.

24. F. Preparata and M. Shamos, Computational geometry: An introduction, Springer-Verlag, New York, 1985.

25. T. Belytschko, Y. Krongauz, D. Organ, M. Fleming, and P. Krysl, Meshless methods: An overview and recent developments, Comp Meth Appl Mech Eng 139 (1996), 3–47.

26. G. Farin, Surfaces over Dirichlet tessellations, Comp Aided Geom Des 7 (1990b), 281–292.

27. D. F. Watson, Contouring: A guide to the analysis and display of spatial data, Pergamon, Oxford, 1992.

28. G. Farin, Curves and surfaces for computer aided geometric design: A practical guide, Second Ed., Academic, New York, 1990a.

29. G. Farin, Triangular Bernstein–Bézier patches, Comp Aided Geom Des 3 (1986), 83–127.

30. C. de Boor, ''B-form basics,'' Geometric modeling: Algorithm and new trends, G. Farin (Editor), SIAM, Philadelphia, 1987, pp. 131–148.

31. W. Böhm, G. Farin, and J. Kahmann, A survey of curve and surface methods in CAGD, Comp Aided Geom Des 1 (1984), 1–60.

32. C. T. Loop and T. D. DeRose, A multisided generalization of Bézier surfaces, ACM Trans Graphics 8 (1989), 204–234.

33. T. J. R. Hughes, The finite element method, Prentice–Hall, Englewood Cliffs, N.J. 1987.

34. R. Sibson, ''A brief description of natural neighbor interpolation,'' Interpreting multivariate data, V. Barnett (Editor), John Wiley, Chichester, 1981, pp. 21–36.

35. G. Farin, ''Smooth interpolation to scattered 3D data,'' Surfaces in CAGD, R.E. Barnhill and W. Böhm (Editors), North–Holland, Amsterdam, 1983, pp. 43–63.

36. S. Agmon, Lectures on elliptic boundary value problems, Van Nostrand, New Jersey, 1965.

37. L. D. Landau and E. M. Lifschitz, Theory of elasticity, Second Ed., Pergamon, Oxford, 1970.

38. P. G. Ciarlet, The finite element methods for elliptic problems, North–Holland, Amsterdam, 1978.

39. D. A. Dunavant, High degree efficient symmetrical Gaussian quadrature rules for the triangle, Int J Num Meth Eng 21 (1985), 1129–1148.

40. J. R. Shewchuk, Triangle: A two-dimensional quality mesh generator and Delaunay triangulator, Sch Comp Sci, Carnegie Mellon Univ, Pittsburgh, PA 15213, 1996b. Available at `http://www.cs.cmu.edu/ ˜ quake/triangle.html`.

41. J. R. Shewchuk, Show me: A display program for meshes and more, Sch Comp Sci, Carnegie Mellon Univ, Pittsburgh, PA 15213, 1996a. Available at `http://www.cs.cmu.edu/ ˜ quake/showme.html`.

42. M. J. M. Bernal and J. R. Whiteman, Numerical treatment of biharmonic boundary value problems with re-entrant boundaries, Comp J 13 (1970), 87–91.

43. J. A. Gregory, D. Fishelov, B. Schiff, and J. R. Whiteman, Local mesh refinement with finite elements for elliptic problems, J Comp Phys 29 (1978), 133–140.

44. S. P. Timoshenko and S. Woinowsky–Krieger, Theory of plates and shells, Second Ed., McGraw–Hill, New York, 1959.

45. J. L. Batoz, K. J. Bathe, and L. W. Ho, A study of three-node triangular plate bending elements, Int J Numer Meth Eng 15 (1980), 1771–1812.

46. B. T. Smith, J. M. Boyle, B. S. Garbow, Y. Ikebe, V. C. Klema, and C. B. Moler, Matrix eigensystem routines—EISPACK guide, Springer–Verlag, New York, 1974.

47. A. W. Leissa, Vibration of plates, NASA-SP-160, Nat Aero Space Admin, 1969.